VIRTUAL COLON UNFOLDING FOR POLYP DETECTION

ZHANG CHENCHEN

(B.ENG., HUAZHONG UNIVERSITY OF SCIENCE AND

TECHNOLOGY)

A THESIS SUBMITTED

FOR THE DEGREE OF MASTER OF ENGINEERING

DEPARTMENT OF ELECTRICAL AND COMPUTER

ENGINEERING

NATIONAL UNIVERSITY OF SINGAPORE

2005

ACKNOWLEDGEMENT

CONTENT

Summary

Colorectal cancer has been among the leading cause for deaths from cancer. Since early detection of lesions can cure the disease or prevent its development into cancer, regular colorectal screening is advocated. Several options exist, all have advantages and disadvantages. The colonoscopy, regarded as "golden standard", provides the most accurate result. However, it is not well accepted among asymptomatic people since it is uncomfortable, time consuming, invasive and risk potential. Virtual colonoscopy, which combines medical imaging with computer graphics technique, is developing as an alternative non-invasive and time-efficient screening.

In this research a virtual colonoscopy system is developed to assist the inspection of the colon. Endoscopic fly-through navigation and virtual dissection of the surface are two modes of visualization, the latter being the focus of this research. Several procedures are included in the development: colon segmentation, medial axis extraction and surface unfolding.

Colon segmentation is not that straightforward because there are fluid residues inside the colon as a result of imperfect bowel cleansing. This induces the partial volume effect. Also in CT images, the intensity of the colon is in the same range as that of some other organs, such as the lungs and small intestine. We combined both thresholding and region growing to solve the above problems.

Medial axis extraction is an essential process because it is both the flying path for

endoluminal navigation and the reference axis for surface unfolding. The method we used is based on distance transform. Two distance transforms are applied. The distance field from a single point allows the extraction of the shortest path, while the distance field from the colon surface pushes the axis away from the surface and ensures the centeredness of the axis.

Surface unfolding is the focus of the system. We propose to first acquire a series of cross-sections and then unfold them onto a plane. The cross-sections are obtained by ray casting starting from the medial axis according to the distance map from the colon surface. A snake algorithm is proposed to refine the contours. The final contours are curved to avoid the intersections. Finally, the cross-sections are projected onto regular grids, and surface rendered into 3D models for inspection.

Experiments were conducted to investigate the performance of the system. Two CT datasets were processed, and both belong to normal patient without polyps. In order to examine the ability of the algorithm to render abnormal structures correctly, synthetic polyps are embedded. Results show that polyps are detectable.

In conclusion, our system is shown to be promising to provide real-time diagnosis of colorectal abnormalities. The system is able to reconstruct the colon in two means and detect polyps larger than 1cm that are of clinical relevance. It will contain all the current modules of virtual colonoscopy after the automatic polyp detection portion is completed.

List of Tables

List of Figures

CHAPTER

1

Introduction

_____

1.1 Background

Colorectal cancer is among the most commonly diagnosed cancers in western countries [1]. A sedentary lifestyle and western-style diet are known to be risk factors, with the risk increasing with age. Colorectal cancers are often diagnosed in the later stage of development because of the insensitivity of the symptoms, which results in a high mortality. Nearly one-third of patients who develop colorectal cancer die of the disease. Deaths from colorectal cancer rank third after lung and prostate cancer for men and third after lung and breast cancer for women in the United States.

Most colorectal cancers start as benign adenomatous polyps, a kind of overgrowth of normal cells. Cells in polyps may continue to grow more out of control, which can take 5 to 15 years for a malignant transformation. This kind of malignant transformation is found in approximately 1% of polyps of less than 1cm in size compared with 10% of

larger polyps [2]. It is generally accepted that early diagnosis and removal of pre-malignant polyps can increase the chance of avoiding or curing cancer, and reduce the mortality from the cancer. Statistics show that the overall incidence of colorectal cancer increased until 1985 and then began decreasing (Fig. 1.1) in the United States. Early detection and removal of polyps is believed to be the most probable reason for such a decrease [3]. Therefore many societies recommend regular colon screening，especially for those over the age of 50 who have high risk to develop colorectal cancer.
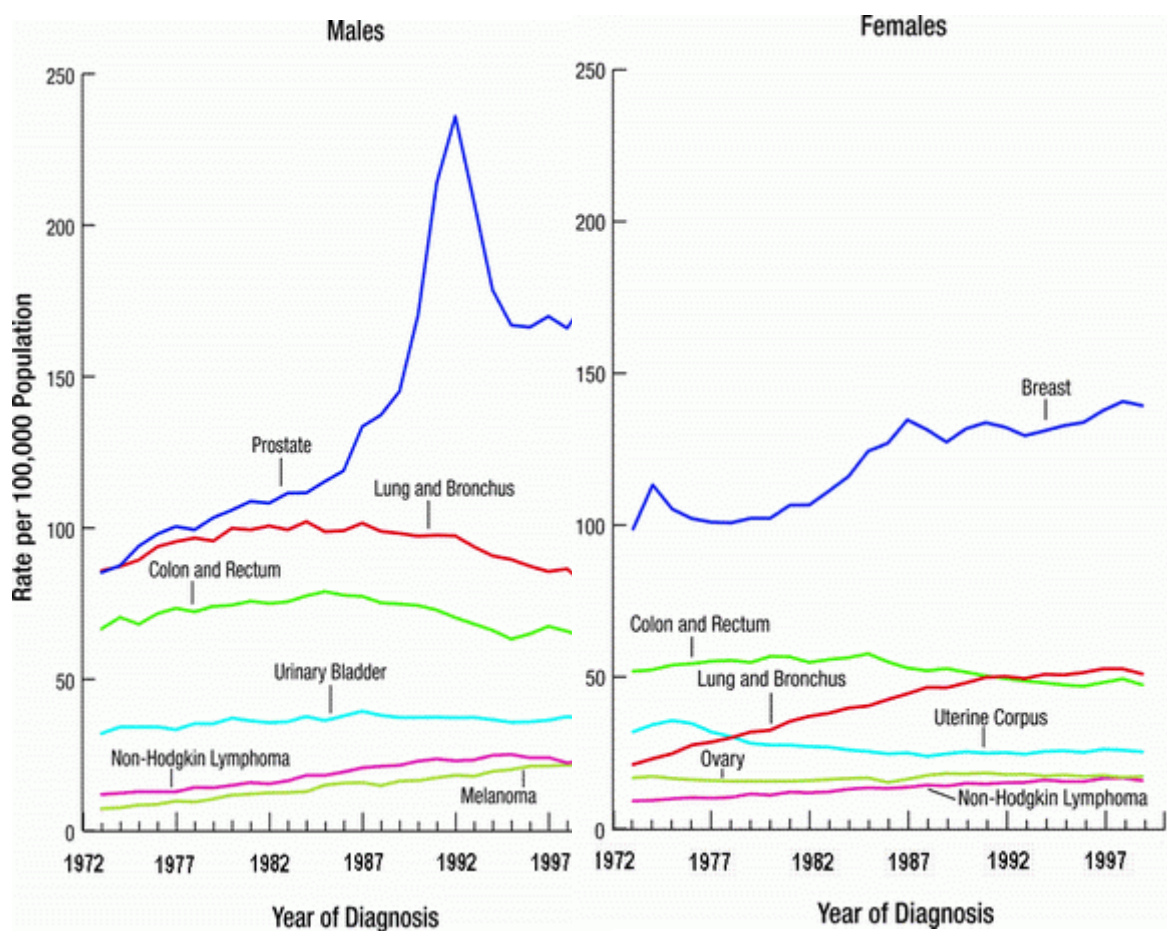
Figure 1.1 Age-adjusted cancer incidence rates[*] among males and females, US, 1973-1999.

*Rates are age adjusted to the 2000 US standard population.

Source: Surveillance, Epidemiology, and End Results program, 1973 to 1999, Division of Cancer Control and Population Sciences, National Cancer Institute, 2002.

1.2 Colorectal Screening

The large intestine begins at the cecum where undigested material is passed into it from the small intestine. The colon follows the cecum, and is divided into the ascending colon, transverse colon, descending colon and sigmoid colon. Excessive water and salt is absorbed in colon, and then remaining waste is converted to feces. The last part of large intestine is the rectum, where feces are stored before being eliminated through anus (Fig. 1.2).
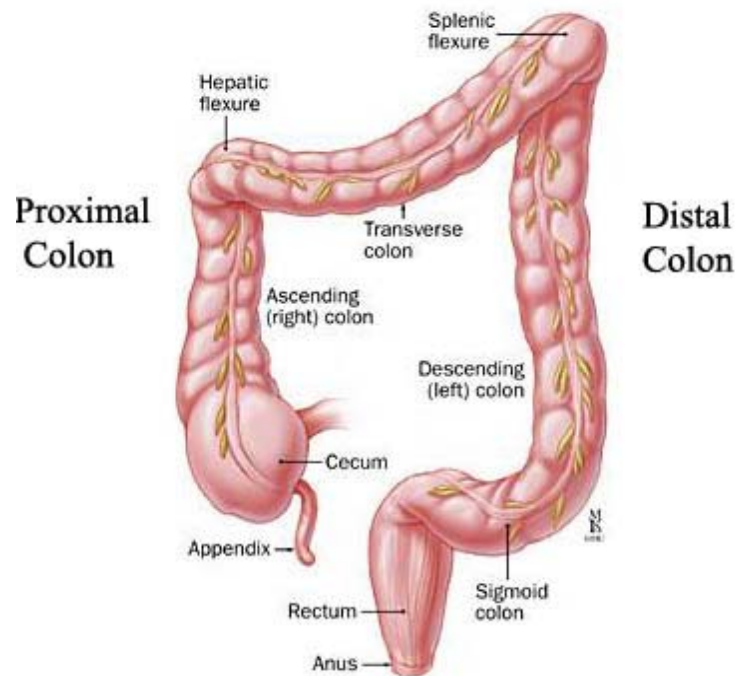
Figure 1.2 Anatomy of the large intestine [4]

The incidence rate of colorectal cancer differs at different portion of the colon and rectum. It occurs most frequently in the proximal colon (right side of the body including the cecum, ascending colon and transverse colon), followed by the rectum, and the least in the distal colon (left side including descending colon and sigmoid colon) [5]. Therefore, a screening procedure that can investigate the entire colon becomes necessary.

Nowadays, several diagnostic procedures exist for colorectal screening. Faecal occult blood test (FOBT) checks the stool for hidden blood, which will not cause bleeding or tear. It helps to detect abnormalities but the accuracy is low. Flexible sigmoidoscopy can effectively reduce the mortality from colorectal cancer, but it is not a total colon screening. It cannot reach the proximal colon, where 40% of cancers occur.

Barium enema and colonoscopy are most commonly used. Barium enema is an X-ray examination after the colon and rectum are instilled with barium sulfate and inflated with air. The procedure is safe, comparatively cheaper and more comfortable than colonoscopy. It allows the viewing of the entire colon and rectum. However, it requires a lot of patient cooperation to obtain images from different views. It requires thorough colon cleansing, and the sensitivity is low. In addition, biopsy is not possible with a barium enema. Therefore additional procedures are necessary if any abnormalities are indicated.

Colonoscopy is regarded as the gold standard for colorectal examination. It is the only available procedure that allows the physicians to look at the inside of the entire large intestine and remove the polyps at the same time. It is performed by inserting a flexible tube (colonoscope) about as thick as a finger into the anus. It is then advanced slowly into the rectum and through the colon under visual control (Fig. 1.3). The colonoscope has lenses and light at the tip so that physician can see what is ahead either through the instrument itself or through a television monitor [6].
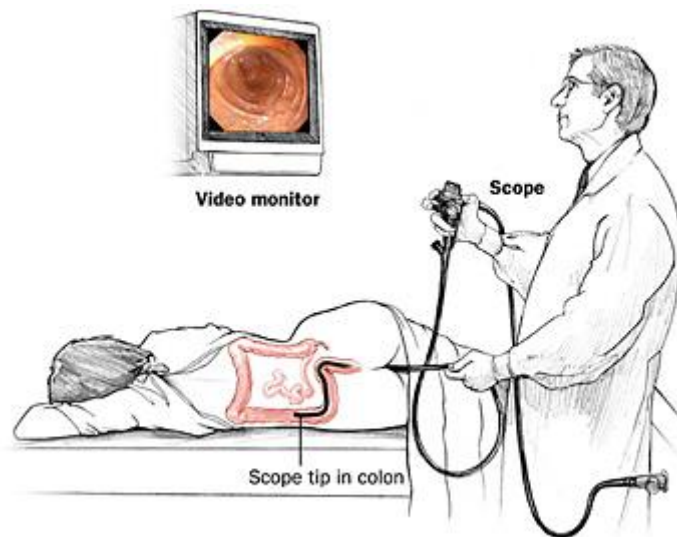
Figure 1.3 Sigmoidoscopy and colonoscopy [4]

In the process of the colonoscopy, if suspicious areas or very small polyps are inspected, the biopsy forceps can take the tissue or remove the polyp (Fig. 1.4), which will be sent to pathologists for microscopic analysis. For large polyps, snare resection with cauterization can directly eliminate them (Fig. 1.5).
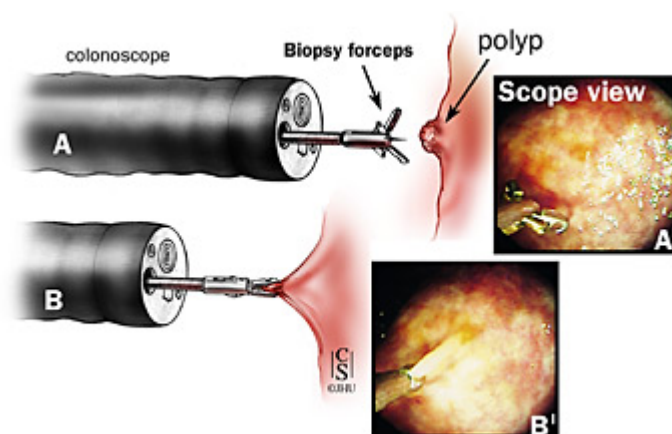
Figure 1.4 Biopsy technique for polyp removal [4]
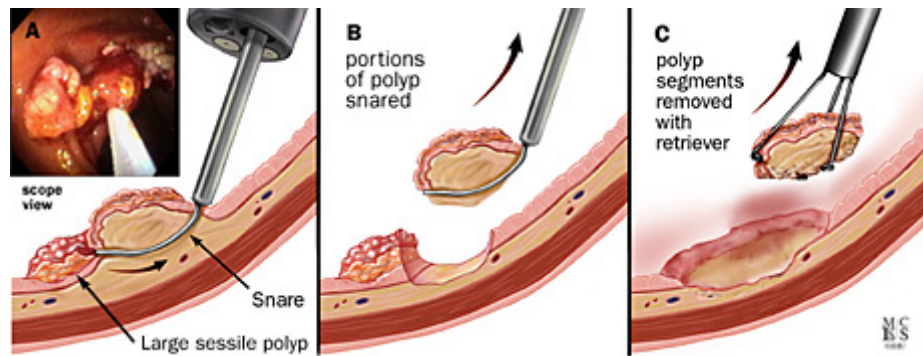
Figure 1.5 Snare resection for polyp removal [4]

Colonoscopy is the most reliable among current available screening procedures. However, colonoscopy fails to examine the proximal colon in about 5-15% of the cases [7]. Besides that, it cannot visualize some of the colon surface because it can only look forward. Bowel preparation and sedation are needed which make patients feel uncomfortable. Although it is a safe procedure, it is invasive and risks of perforation exist. The procedure usually takes 15 to 60 minutes, and the expense is high. Due to the above drawbacks, many asymptomatic people feel reluctant for such a screening. Thus, a technique that is non-invasive, accurate, comfortable, and cost-effective is valuable and attracts lots of research interest.

Virtual colonoscopy (also named computed tomography (CT) colonography) is an alternative new technique for the screening of the large intestine. It is an imaging technique that combines volumetrically acquired CT scan data with computer graphic software to generate two-dimensional (2D) and three-dimensional (3D) views of the colon. Bowel preparation is required, but sedation is not needed. A colonoscope is not needed so that it is non-invasive and well tolerated. The process takes less time than conventional colonoscopy.

The most common visualization technique in virtual colonoscopy is the simulation of the conventional colonoscopy which provides 3D endoluminal reconstructions (Fig. 1.6). It is formed by surface rendering or volume rendering techniques. Perspective projection and real-time rendering are performed to fly through the colon lumen, which is similar to the advancement of the real colonoscope inside the colon. When a suspicious structure is found, view directions can be adjusted locally for further inspection. Retrograde viewing is also enabled, which conventional colonoscopy cannot afford. In addition, 2D axial images can be combined for confirmation. Many software packages have been developed to provide endoluminal navigation of the colon.
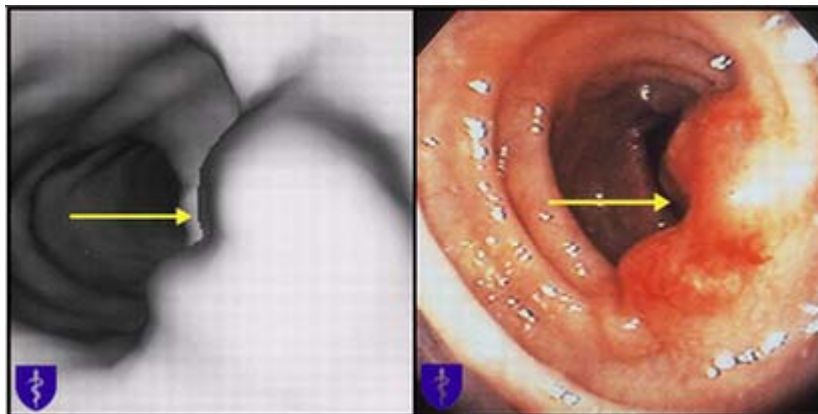
Figure 1.6 Virtual colonoscopy (left) and conventional colonoscopy show a cancerous mass (arrow) [8]

One disadvantage of CT colonography is the exposure to radiation. Currently, various groups of researchers are looking at magnetic resonance (MR) colonography, which is radiation free. In addition, because MRI is able to visualize contrast in soft tissue, it is promising in producing images with more details such as the structures behind the colon wall. However, due to the lower resolution and the high cost of MR scanning, CT will still remain as the main imaging modality for virtual colonoscopy.

Although the fly-through endoluminal navigation provides different view direction of the colon surface, it could still suffer from the coverage deficiencies of the surface due to colon tortuosity. Moreover, the generation and inspection of the fly-through navigation is time-consuming. Many physicians find the investigation process to be tedious. A new display technique called virtual dissection has been developed to avoid the above problems. Virtual dissection aims to open and flatten the colon so that the entire surface is presented as a single or a few images. This will save much time and obtain more surface coverage for the examination.

Besides all of the screening techniques along with inspection by the radiologist, efforts have being made to let computer perform the same task as the radiologist. Computer aided diagnosis (CAD) is such a technique merged with virtual colonoscopy to automatically detect polyps by use of different information about polyps, folds and surrounding structures in the scanned data, such as size, shape and curvature. CAD system is under research for improvement in sensitivity and specificity. If CAD can be effectively developed, the diagnosis process will be much faster, and more potential areas can be detected.

1.3 Project Overview

In order to reduce the incidence and mortality of colorectal cancer, people older than 50 and those with family history are strongly suggested to do regular screening. Due to the discomfort, embarrassment and risk accompanied with colonoscopy, it is essential to develop a technique that is non-invasive, comfortable and accurate. Then, there will be more people willing to adopt colon inspection. Virtual colonoscopy has the potential

of being such a technique. Though some studies [9, 10] reported lower rates for polyp detection by virtual colonoscopy than by conventional colonoscopy, many others find that the performance of virtual colonoscopy is comparable with the conventional colonoscopy [11, 12], especially for clinically significant polyps (larger than 10mm) [13, 14].

Our project aims to develop a virtual colonoscopy system which is used to facilitate clinical diagnosis for colorectal abnormalities. This project is an extension on the final year project of another student, Yeo Eng Thiam. This system is able to segment the colon from 2D abdominal CT images and automatically generate the fly-through path (median axis of the colon). For diagnostic purposes, fly-through visualization and virtual dissection are both developed. A fly-through provides different view direction of the colon surface which is very similar to that from real colonoscopy. Virtual dissection provides another diagnostic means similar to pathology where radiologists are able to inspect the entire surface at a time. Virtual dissection is the main focus of this thesis. We obtained 2D abdominal CT images from National University Hospital (NUH) of Singapore. As data of patient with positive diagnostics is not available, we embed synthetic polyps for testing. Finally, there is a concurrent final year project, by Ng Ting Ting, which aims to develop automatic polyp detection for the virtually dissected colon. Once the entire system is developed, it will be placed in NUH for trials and evaluation. The entire system is developed on Visual C++, OpenGL, C.Net using a P4 2.4GHz machine.

1.4 Thesis Organization

The thesis is divided into 8 chapters:

Chapter 1 is a brief introduction to the background and the motivation of colorectal screening techniques. Project overview is presented, and organization of the thesis is also included.

Chapter 2 presents an overview of virtual colonoscopy technique. It also reviews approaches for different phases of virtual colonoscopy, i.e., colon segmentation, medial axis extraction and surface unfolding.

Chapter 3 provides an overview to the system. Procedures for virtual colonoscopy will be described, including patient preparation, image acquisition, etc. Then a detailed flow chart of the project is presented.

Chapter 4 describes the characteristics of CT images, which is essential for the following segmentation of colon. Then it will illustrate optimal adaptive thresholding method for initial segmentation, and explain the approaches for partial volume effect removal and region growing of the segmentation process. Surface rendering for 3D virtual model generation will also be covered.

Chapter 5 describes the approach for medial axis extraction. The distance transform method used in our project is described in detail. Post-processing including axis refinement, connection and smoothing will also be briefly discussed. Finally, results will be presented.

Chapter 6 presents the algorithm for colon surface unfolding. The method to obtain cross-sections is described, and then the processing to flatten and straighten the colon is elaborated. The chapter concludes with samples of unfolded colon surface.

Finally, the polyp detection results with discussion will be presented in Chapter 7. We conclude in Chapter 8 with suggestions for future work.

CHAPTER

2

Literature Review

_____

2.1 Virtual Colonoscopy

Virtual colonoscopy was first presented in 1994 by David Vining, who simulated the endoluminal view of optical colonoscopy from CT volumetric data [15]. Different names were proposed for this technique, such as virtual colonoscopy, 3D colonoscopy, CT colonoscopy, CT pneumocolon, CT colonography, but CT colonography is accepted as the most suitable term [16]. Since the technique is not constrained to CT data (MRI data and ultrasound data are also processed), CT colonography may not cover the field of its application. Virtual colonoscopy, as an initially proposed term, is also very common because of its high-tech connotation, though strictly it should be reserved for the simulated fly-through navigation inside the colon, which does not take the new visualization of virtual dissection into consideration. Whatever the name, the technique describes the same method of constructing various 2D and 3D visualization

of the colon from volumetric scan data for the purpose of colorectal screening and diagnosis. Virtual colonoscopy has attracted tremendous research interest since it was introduced. The first commercial product, the Navigator (GE Medical Systems, Milwakee, WI), was presented in 1995. Nowadays, more than 20 virtual colonoscopy systems have been developed.

Many studies have been carried out to evaluate the feasibility and the performance of virtual colonoscopy. MR colonography shows a high sensitivity (the percentage of affected patients recognized by the clinical test) and specificity (the percentage of healthy subjects recognized by the clinical test) from some studies [17, 18], but it is primarily used in Europe and not well accepted in other countries. Most studies are focusing on CT colonography. Some are based on supine or prone scanning only, whereas most are using dual position scanning. The study by Yee et al. [19] shows that sensitivity for polyp detection is significantly improved by combing supine and prone scanning.

From some studies applying dual position scanning, virtual colonoscopy was performed before conventional colonoscopy at the same day. The interpretation of virtual colonoscopy generally includes 2D axial images, sagittal and coronal reformations and 3D endoluminal images. The sensitivity is dependant on polyp size. When using a per-polyp matching scheme, some investigations [9, 10] showed a sensitivity of 73%-75% for polyps $\geq$ 10mm and 22%-47% for polyps of 6-9mm. However, other studies [11, 12] suggested a sensitivity of 90%-91% for polyps $\geq$ 10mm, 80.1%-82% for intermediate-sized polyps, and 55%-59.1% for polyps < 5mm. Moreover, most studies [11, 12, 13, 14, 20] acquired sensitivity (per-polyp) of

90%-100% for polyps larger than 10mm. For specificity on a per-patient basis, many studies [10, 11, 12] show good result (90% or above) for polyps ≥ 10mm, while several are lower (around 75% [10, 12]) for polyps ≥ 5mm. The result of investigations varies. Oral contrast agent has been proposed to be applied with bowel preparation as an approach to improve the sensitivity of polyp detection. The consideration is that the difference between polyps and fluid residues will be enhanced as a result of contrast medium, and hence the sensitivity may be improved. A study by Vining [21] demonstrated an increased sensitivity, while another investigation [10] did not. Therefore, this technique is still under evaluation.

On the other hand, many factors may influence the performance of virtual colonoscopy compared with conventional colonoscopy, such as lower image resolution, faecal residues resulting from suboptimal bowel preparation and insufficient experience of the radiologists with the diagnosis procedure [22]. The problem of inter-observer and intra-observer variance is referred to as the "learning curve" for reading virtual colonoscopy. It is well recognized that radiologists should undergo rigorous training to reach proficiency.

Although the sensitivity and specificity are poor for polyps of 5mm or smaller, and moderate for polyps of 6-9mm, the performance of CT colonography for larger polyps is much better and comparable to conventional colonoscopy. In addition, small polyps are of little clinical relevance because polyps < 10mm have little probability to develop into cancer. Even if they will turn cancerous, the time is estimated to be about 10 years [23]. Virtual colonoscopy has already been used in some institutions [24]. Currently the clinical use of virtual colonoscopy is for patients who undergo incomplete

colonoscopy, patients who have obstructing lesions, and patients who are not suitable for colonoscopy due to contraindications or other medical reasons. With technical development in software and hardware and increased expertise of radiologists, the performance for medium and small-sized polyp detection will be greatly improved. Many researchers [24, 25] agree that virtual colonoscopy has enormous potential to be widely accepted as an alternative to other diagnostic tools.

Some studies [26, 27] also compared the performance of common fly-through navigation with their new method which presented a full 360 degree view in unfolded cubes along the central path. The unfolded view has shown a reduction in inspection time and a slightly higher sensitivity than the fly-through navigation with more percentage of surface visualized. The result is quite impressive, and this area is under research.

Several steps are involved in virtual colonoscopy: image data acquisition, segmentation for isolating colon, generation of flying path, rendering for visualization, fly-through navigation, new-evolving colon surface unfolding and computer aided diagnosis. In the following section we will elaborate the modules that are most relevant to the work in this report.

2.2 Segmentation

Segmentation has applications in many areas, and it is an important pre-processing step in virtual colonoscopy. Usually the intensity range in CT abdominal images consists of three regions corresponding to air, soft-tissue and high density structure

(fluid, bone). Thresholding is the simplest approach, which is used to classify the region of interest based on image intensity difference between different materials. There are a few problems with a direct thresholding approach. Partial volume effect will cause mis-segmentation. In addition, the similar intensity of colon fluid and bone, together with the similar intensity of colon air and lung, stomach, large intestine, makes several unwanted structures to be segmented out with colon. Morphological operation is another method, but seed points need to be planted in every region of interest, which includes too much user intervention and is very troublesome [28]. Ideally, thresholding combined with morphological operation and connected component analysis can produce good segmentation results [29].

The segmentation process can be manual, semi-automatic and automatic. Manual segmentation requires lots of user interaction, so it is tedious, time-consuming and leads to variable accuracy with different operators. Semi-automatic segmentation needs some degree of user intervention, such as threshold and seed point setting. For automatic segmentation, the accuracy decreases since almost all the current automatic algorithms cannot achieve the same accurate result as the manual segmentation [30]. But the automatic mode is the most convenient, and is desired by users. Thus, many researches focus on semi-automatic and automatic algorithms.

Wyatt et al. described an automatic segmentation, but their result was not accurate and the process took 60-65 minutes which is too slow [31]. Another approach using principal component analysis by Chen et al. [32] was faster but still computationally intensive. Other researchers in SUNY Stony Brook [28, 33, 34] also presented some automatic segmentation approaches, one of which used segmentation rays and the

other used a vertical filter for partial volume effect removal. The results are satisfactory and time-efficient.

The problem remained in segmentation is that there is some situations in which the colon touched itself or the lung. In this case, the boundary will be removed and the neighboring regions will be classified as one connected region. Thus the shape of the colon at the boundary will be lost. In the worse situation, the lung is segmented together with the colon as the lung is within the same intensity range as the colon.

2.3 Centerline Extraction

After constructing a 3D model of the colon, it is essential to generate a flying path for endoluminal navigation and colon unfolding. The centerline of the colon lumen is regarded as an appropriate path, which consists of a group of connected points from one end to the other end of the colon body. To be well fitted for the fly-through navigation, the medial axis should be one-voxel wide without self-intersection. And it should stay away from the colon wall as far as possible to prevent the navigator from penetrating the colon wall or hugging the corners. Due to the complicated shape of the colon, centerline extraction has been a challenging task. Extensive work in this area is mainly in three categories: manual extraction, topological thinning and distance transform.

Manual extraction requires significant user interaction. Some key points are defined by radiologists, and then approximated to be a connected path using interpolation or curve fitting [35, 36]. This kind of method is quite slow and tedious. Moreover, manual

selection is inaccurate and cannot guarantee that the interpolated path is inside the colon lumen. Therefore, research has been focused on topological thinning and the distance transform.

Topological thinning is considered to provide the most accurate result. It peels off the object layer by layer until the skeleton remains. In the process, end points should be retained to ensure that the topology is preserved. This iterative algorithm is very computationally intensive, so some optimization techniques have been developed to speed up the algorithm. Ge et al. [37] presented an approach using downsampling to increase efficiency. This indeed accelerates the process, but downsampling leads to a lower accuracy. Another approach [38] tried to separate the thinning from connectivity analysis. It extracted an initial candidate axis on the surface followed by parallel thinning to relocate the axis, which improved the efficiency and gave an accurate and connective result. Bouix et al. [39] proposed an algorithm to incorporate the average outward flux on the basis of Euclidean distance from the object boundary. Their approach guaranteed connectivity, centeredness and computational efficiency.

The distance transform is considered to be the fastest method. The first step is to calculate for every voxel inside the object its distance from a reference point specified by user. The distance is called distance from starting point (DFS-distance). The next step is to extract a shortest path from another specified end point to the reference point based on the distance map. Several algorithms differ in the distance metric they applied, that is, to define different distance value between a voxel and its orthogonal, 2D diagonal and 3D diagonal neighbors. The Euclidean metric is the most accurate, but many approximate metrics have been proposed to improve computation efficiency,

such as 1-0-0 Manhattan metric [40], 1-2-3 metric [41], 3-4-5 Chamfer metric [35], and 10-14-17 metric [42].

Distance transform method can extract the shortest path, but the path tends to hug the corner at the place of sharp bending. Thus, some researchers tried to improve the centeredness by introducing another distance transform, the distance from the colon boundary (DFB-distance). Zhou et al. [41] proposed an algorithm to replace the points on the shortest path by the voxels of the maximal DFB-distance inside the cluster of the same DFS-distance, obtaining a centered axis but needing some post-processing for connectivity. An efficient approach proposed by Bitter et al. [43] tried to extract the minimum cost path according to the penalized distance, which is based on their new definition of a skeleton. Another algorithm [44] gave a different definition of the centerline and used different weight when computing minimum cost, which further improved the centeredness and computational efficiency.

2.4 Fly-through Navigation

3D visualization of the volume data can be achieved by either surface rendering or volume rendering technique. Surface rendering extracts the geometric iso-surface by applying thresholds to the data so that voxels within the thresholds are retained. It is computationally efficient, but with some accuracy loss. While volume rendering displays the entire range of voxels within a volume without extracting a representative surface. The high quality is attractive, but the computational expense is too high to afford real-time rendering. Many improvements have been made to speed up the rendering.

The modes of navigation differ in how the camera is controlled. For manual navigation, the user has full control of the camera. However, this requires the greatest amount of user intervention, and the user may lose the direction in the process. Automatic navigation is totally free of user interaction, in which the camera moves along the medial axis of the colon lumen. But the radiologist cannot stop at suspicious area for further inspection, so that more work is needed to acquire desired result. Therefore, interactive navigation is more user-acceptable, combing the advantages of the former two modes.

Endoluminal navigation has shown its effectiveness in detection of polyps. However, it suffers from the insufficient coverage the surface (Fig. 2.1). Thus, effort has been made to explore new visualization techniques, such as "unfolded cube" and virtual dissection.
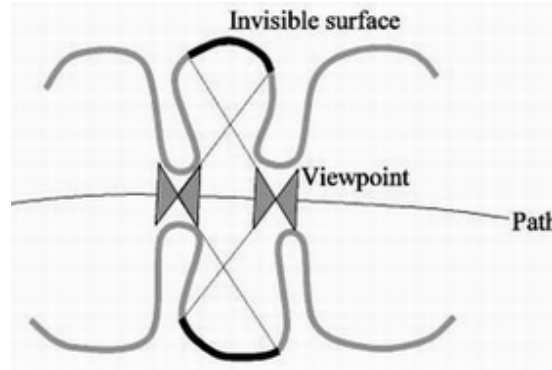
Figure 2.1 Invisible areas in fly-through navigation [27]

2.5 Virtual Dissection

Virtual dissection has evolved as an alternative visualization technique to fly-through navigation. Most of the approaches start with the medial axis inside the colon lumen. In Wang et al.'s algorithm [45], a series of planar cross-sections perpendicular to the

path was calculated, which was named "hard" straightening. Then the cross-sections were piled up and unfolded to generate a flattened colon surface. However in high curvature regions, the neighboring cross-sections tended to intersect or be far away from each other, which might cause double appearance of polyps or missing polyps. They tried to solve this problem in their later work [46]. Here they presented a soft unraveling algorithm to acquire curved cross sections. The cross sections were guided by a virtual electrical field from the locally charged central path. The curved cross sections would avoid intersection if the entire path was charged. But due to its high computational lost, they tended to locally charge the path to decrease at the expense of possible confliction. Wang et al. [47] developed a fast algorithm based on their previous work, which accelerated the process by interpolating representative electric force lines.

Another approach by Haker et al. [48] differs with others because it does not need a medial path. It used conformal mapping, which preserved angles, to map the surface onto a planar rectangular. This method requires a highly accurate segmentation.

The flattening algorithm by Bartroli [49] directly projects the colon surface onto cylinders. They exploited two sampling schemes, constant angle sampling and perimeter sampling. The result is a video of locally flattened surface along the medial axis, which cannot give a complete view of the colon. They further developed another approach [50] which avoided the occurrence of cross section intersection by introducing nonlinear ray casting. The rays were casting out from the central path based on the distance transform from the boundary, which also acquired curved cross sections.

We have reviewed numerous existing algorithms for the virtual colonoscopy. Lots of research effort has been made on the various components for this task, these include segmentation, medial axis extraction, fly-through visualization and virtual dissection. Currently, there are also many virtual colonoscopy systems, which are capable of fly-through navigation mode. However, there is still no clinical system providing the unfolded view of colon surface, which is a crucial technique to speed up the diagnosis process. Therefore, the aim of this project is to firstly design such a system that is able to provide all the above modules for clinical use. Algorithms are selected for each module and customized to obtain the comparable result to the independent algorithms, and finally fine tuned to complete an integrated system. The system will be placed in hospital for trials, and subsequent refinement will be made accordingly. We plan for it to be eventually deployed in clinical diagnosis.

CHAPTER

3

System Overview

_____

In this chapter, the overview of the virtual colonoscopy system we have developed is presented. The system consists of several modules as depicted in Figure 3.1.
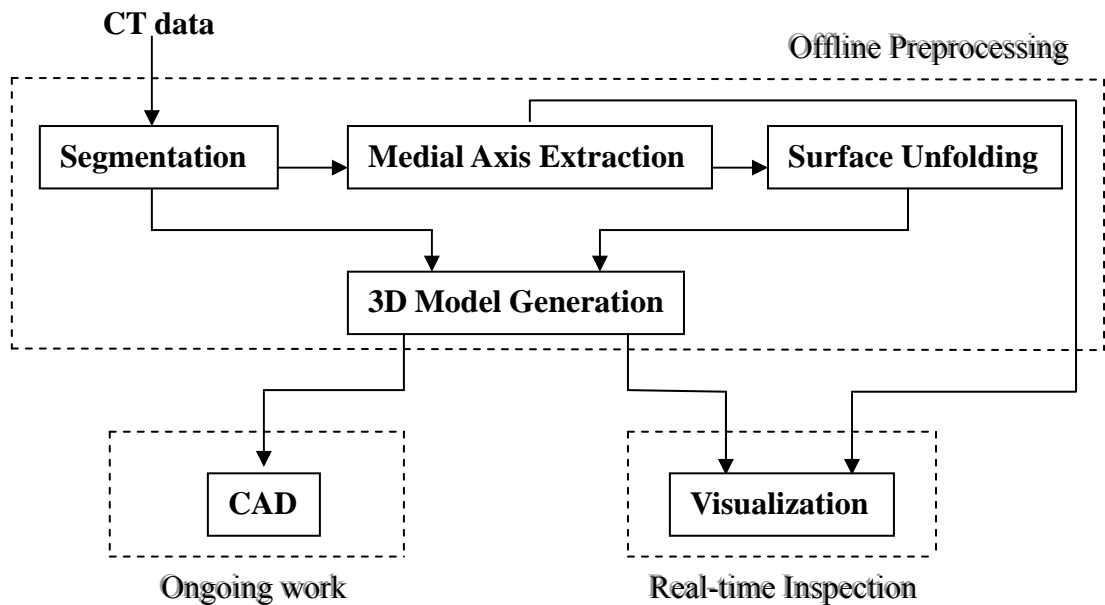
Figure 3.1 Modules in the virtual colonoscopy system

The entire system is divided into two portions: offline processing and real-time visualization. Given the CT image data, offline processing undergoes several modules. The final outputs are the fly-through path, the VRML model for 3D colon and the unfolded colon surface, which will be opened in the visualization module displaying the fly-through navigation and the unfolded view.

The detailed flowchart of the system is illustrated in Figure 3.2. The following paragraphs give a brief walk-through on the functional aspect of the system.

To ensure a successful colonography, adequate patient preparation is required. The bowel cleansing regimes are administered similarly to those used for conventional colonoscopy, which usually starts on the day before. Prior to scanning, a rectal tube is inserted and the large bowel is insufflated with gas to ensure an optimal colonic distension. Room air or carbon dioxide is usually pumped in to the extent of patient tolerance, the latter being more comfortable and more expensive. Once the preparation is well done, the high-resolution CT images of the patient are acquired within one single breath-hold to prevent motion artifacts.

After image acquisition, segmentation, medial axis extraction and unfolding are performed, each of which will be elaborated in the following chapters. When the segmented colon data and unfolded surface data are ready, the VRML model is generated for visualization.
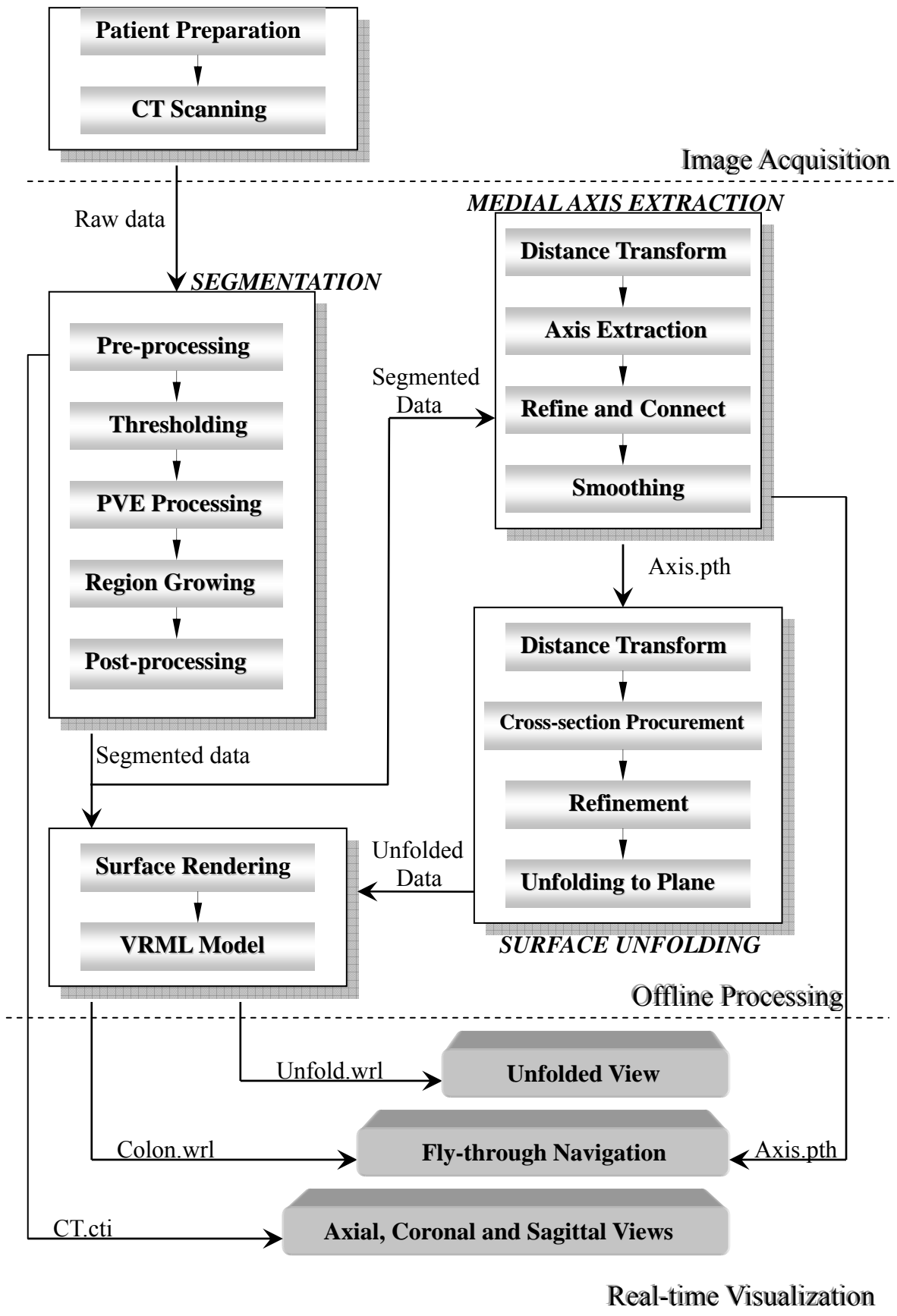
Figure 3.2 Detailed flowchart of the system

In the visualization module, three forms of display are provided: 2D CT images, endoscopic view and unfolded view. Figure 3.3 shows the corresponding screens. The visualization is implemented using OpenGL, OpenGL Utility Toolkit (GLUT), and GLUI (GLUT-based C++ graphical interface library). The fly-through navigation is developed by Yeo Eng Thiam [51]. This report will focus on the surface unfolding portion.
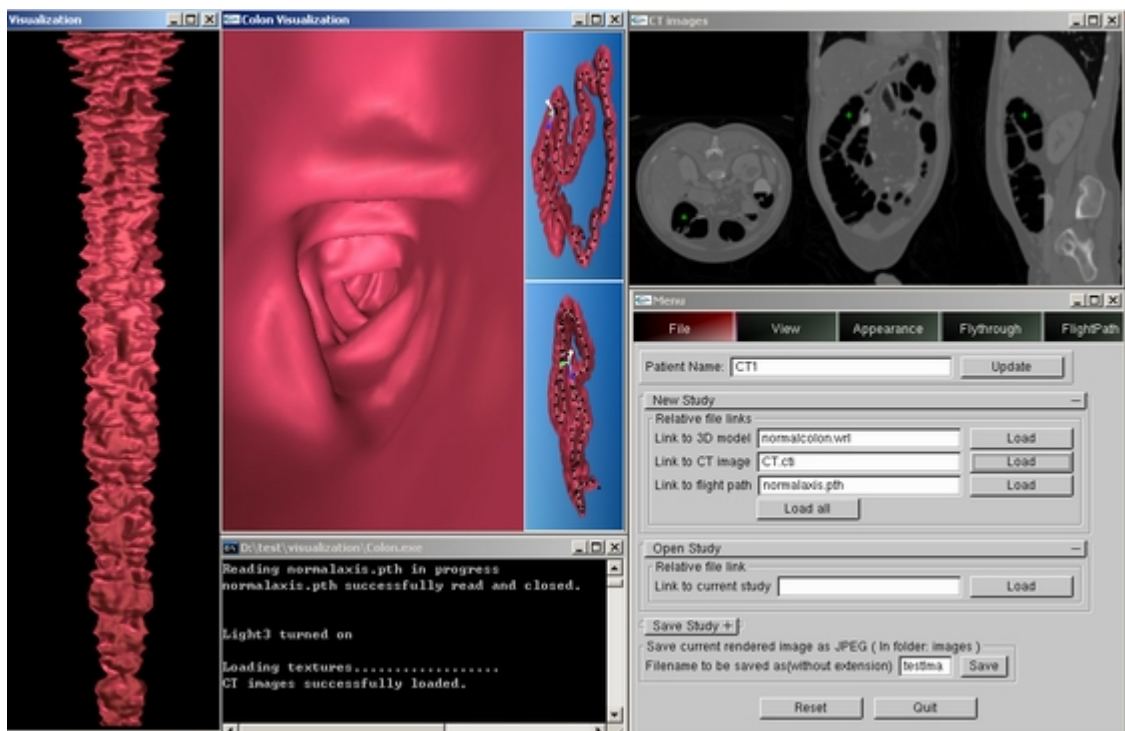
Figure 3.3 Visualization screens: unfolded view (left), endoscopic view (middle), 2D axial, coronal and sagittal views (right).

All the above visualization modes aim to assist the radiologists for colorectal inspection. Computer aided diagnosis is a new research topic that may enhance the efficiency and accuracy. The work on automatic polyp detection, an ongoing project by another student Ng Ting Ting, is yet to be included in the system.

CHAPTER
4

Colon Segmentation

_____

In this chapter, we describe the method used to segment the colon from the original CT dataset. The next section will cover the specifications of the CT dataset. Sections 4.2 and 4.3 present the segmentation algorithm and the surface rendering module. The last section shows the results and its 3D visualization.

4.1 Characteristics of CT Images

The dataset for this project comprises a series of CT slices covering the abdominal area. Each slice is a 512x512 image with 12-bit pixels. This dataset is in DICOM format with scanning settings (i.e., slice thickness, image resolution, field of view and image ordering number) stored in the header section of each image (Fig. 4.1(a)). In order to facilitate subsequent processing, the header section is removed from the original data.

| | (a) | (b) |
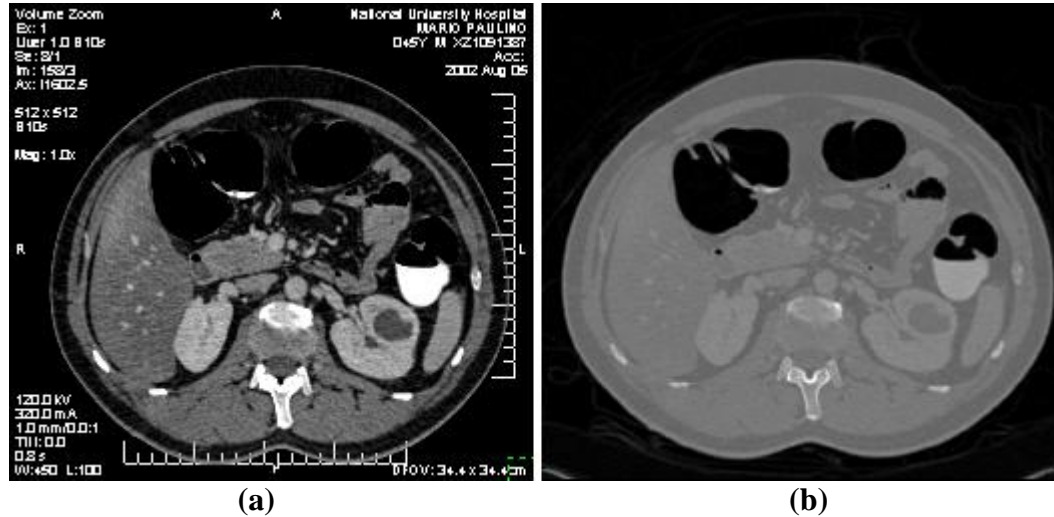
Figure 4.1 (a) CT image in DICOM with header information, (b) corresponding image without header information

The CT slices are stacked to generate a volume according to the ordering number of each slice. The volume data is represented in terms of voxels, which are usually non-isotropic due to the difference in the in-plane and the through-plane resolution of a CT acquisition. As most image processing algorithms prefer the resolution of the dataset to be isotropic, the CT datasets used in this project are resampled to have an isotropic resolution.

The CT image is a cross-section of the body in which matter that attenuate the X-rays more strongly appear brighter than those that attenuate less. Accordingly, bone is the brightest, fat and soft tissue is in the range from dark gray to light gray, while the air in bowel and lung is the darkest (Fig. 4.1). This characteristic provides the basis for separating the air in the colon from the rest of the image.

4.2 Algorithm Description

As explained in section 2.2, simple thresholding or region growing cannot obtain an optimal segmentation due to the partial volume effect and equivalent intensity range among several tissues. Hence, we combine the two approaches to solve the above problems.

4.2.1 Thesholding

Different tissues correspond to several intensity ranges in the CT image. As shown in Fig. 4.2(a), the representative areas are colon air, soft tissue, fluid residues and bone. The histogram of this image is depicted in Fig. 4.2(b).
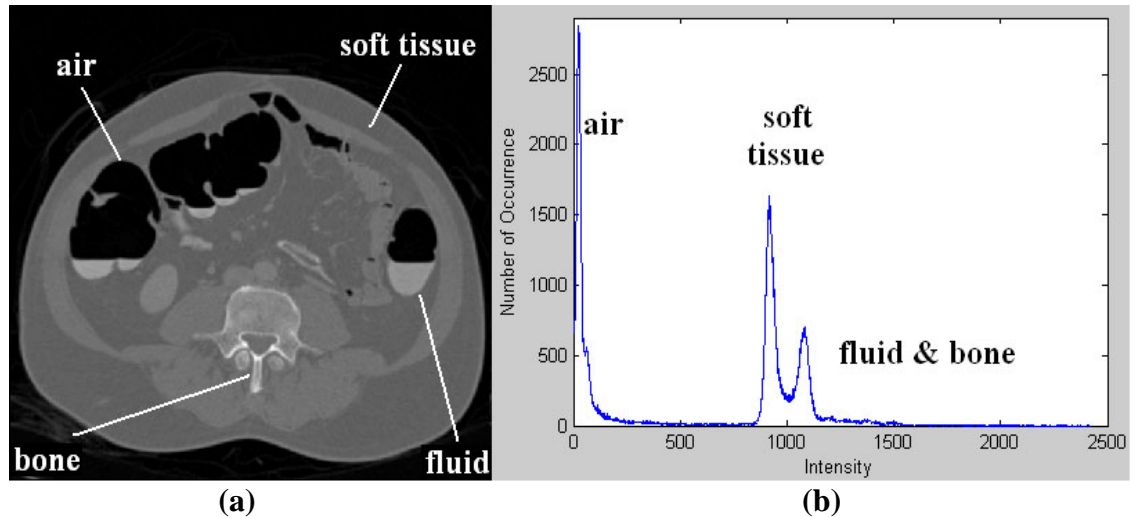
Figure 4.2 The 238th slice (a) intensity of different tissues, (b) corresponding histogram

From the gray-level histogram, a single threshold is not sufficient as we want to not only partition the bowel air from the soft tissue, but also extract the fluid residue. As a result, two-level thresholding is needed. However, as seen in Fig. 4.2(b), due to the significant intensity overlap, it is not easy to decide on an optimal threshold value

between soft tissue and fluid residues.

Our method is based on the optimal global and adaptive thresholding scheme, whose principle is to estimate the threshold by minimizing the average segmentation error. Suppose the image has two gray-level regions: object and background. The histogram may be used as an estimate of their probability density function $p(z)$ (z denotes gray-level values) by viewing z as a random variable. $p(z)$ is the sum of two densities $p_1(z)$ and $p_2(z)$ which corresponds to object and background, respectively (Fig. 4.3). Then,

$$p(z) = P_1 p_1(z) + P_2 p_2(z) \qquad (4.1)$$

where P_1 and P_2 are the probabilities of the occurrence of the two groups of pixels. Further,

$$P_1 + P_2 = 1 \qquad (4.2)$$
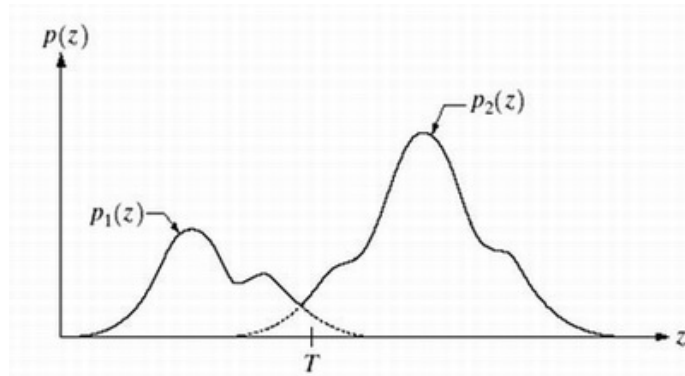
Figure 4.3 Gray-level probability density functions of two groups [52]

Suppose all pixels with gray levels greater than a threshold T belong to background, and the leftover pixels belong to object. Then, the probability of erroneously classifying a background pixel as an object one is

$$E_1(T) = \int_{-\infty}^{T} p_2(z)dz \qquad (4.3)$$

Similarly, the probability of erroneously classifying an object pixel as a background pixel is

$$E_2(T) = \int_T^\infty p_1(z)\,dz \qquad (4.4)$$

Then the total probability of error is

$$E(T) = P_2 E_1(T) + P_1 E_2(T) \qquad (4.5)$$

$E(T)$ is minimized to obtain the threshold T by differentiating $E(T)$ with respect to T and equating the result to 0. The result is

$$P_1 p_1(T) = P_2 p_2(T) \qquad (4.6)$$

Usually, the probability density functions are assumed to be Gaussian.

$$p(z) = \frac{P_1}{\sqrt{2\pi}\,\sigma_1} e^{-\frac{(z-\mu_1)^2}{2\sigma_1^2}} + \frac{P_2}{\sqrt{2\pi}\,\sigma_2} e^{-\frac{(z-\mu_2)^2}{2\sigma_2^2}} \qquad (4.7)$$

where μ and σ are the mean and variance of the Gaussian density. Applying this equation to Eq. (4.6), and the solution for the threshold T can be obtained by solving the following quadratic equation:

$$AT^2 + BT + C = 0 \qquad (4.8)$$

where $A = \sigma_1^2 - \sigma_2^2$

$$B = 2(\mu_1 \sigma_2^2 - \mu_2 \sigma_1^2)$$

$$C = \sigma_1^2 \mu_2^2 - \sigma_2^2 \mu_1^2 + 2\sigma_1^2 2\sigma_2^2 \ln(\sigma_2 P_1 / \sigma_1 P_2)$$

According to the above equation, a threshold T can be calculated to separate two groups. By extending the above method to our problem, we apply a two-level thresholding. The relationship of three intensity regions are: air in bowel and lung (class 1) < soft tissue (class 2) < fluid and bone (class 3).

We have developed a segmentation module which will first determine the threshold T_{low} to separate air in bowel from soft tissue. The interface is user-friendly, which directs the user to select regions corresponding to air and soft tissues. An example of selecting the air region is shown in Fig. 4.4, where the pixels inside the white polygon are selected as a sample set. Then each sample set is used to estimate the probability density function, thus obtaining its mean and variance. Here P_1 and P_2 in Eq. (4.8) are assumed to be the same since the two groups are thought to have equal chance of occurrence in the image. At last, T_{low} can be obtained by solving the Eq. (4.8). For the threshold T_{high} between fluid and soft tissue, the same procedure is used.
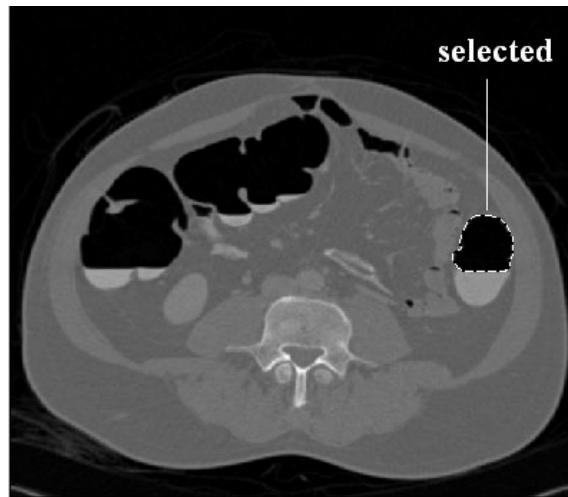
Figure 4.4 Selected samples of colon air class

After obtaining the threshold T_{low} and T_{high}, a two-level thresholding scheme is applied to the dataset. If the gray-level of a pixel is above T_{low}, the pixel is classified as background. The pixels with intensity below T_{low} will be segmented out as "air data", which includes colon air, lung and small intestine. Similarly, when the gray-level of a pixel is below T_{high}, the pixel belongs to background. And the pixels with gray- level above T_{high} are classified as "water data", which usually includes fluid residue and bones. An example of "air data" and "water data" corresponding to the 238th slice in

Fig. 4.2 is shown in Fig. 4.5.
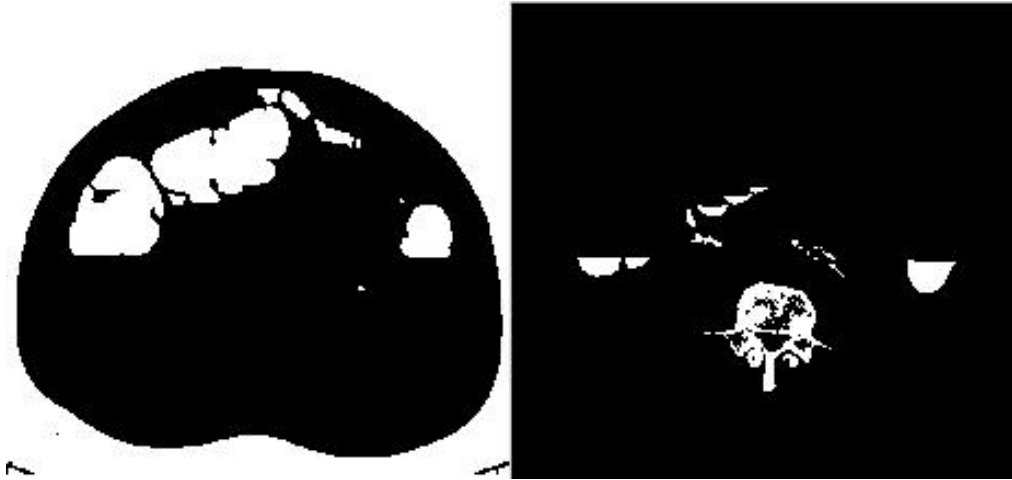
Figure 4.5 "air data" (left) and "water data"(right) of the 238th slice

4.2.2 Partial Volume Effect Removal

Pixels at the boundary between structures contain a mixture of materials, and consequently have an intermediate intensity between the intensity values of the structures. This phenomenon is the partial volume effect (PVE). Here PVE arises at the boundary of region between colon air and colon fluid, because sharp discontinuity of gray-level does not exist at the boundary (Fig. 4.6). The boundary region is not classified into either group, so a gap between the air and fluid regions exists (Fig. 4.7).
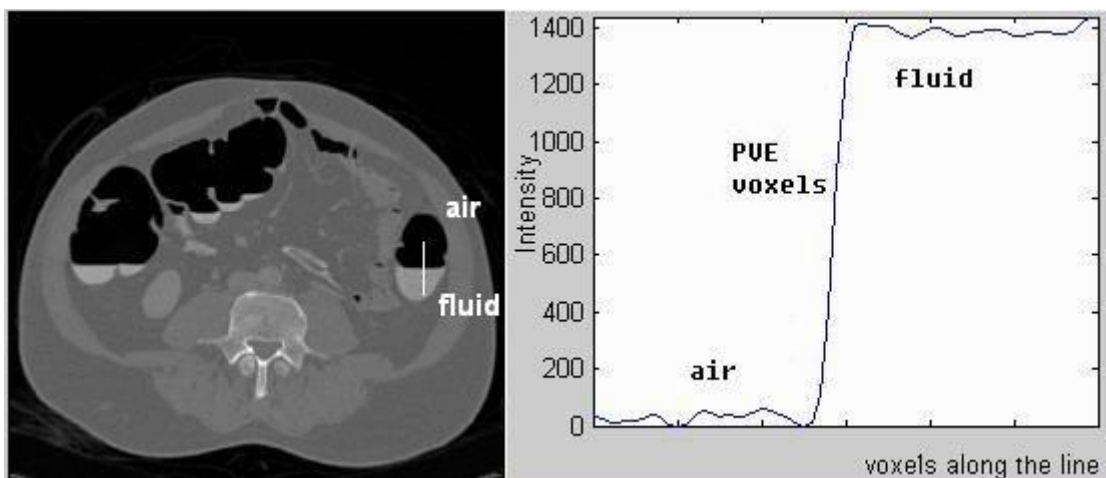
Figure 4.6 Intensity profile along the vertical line from air to fluid
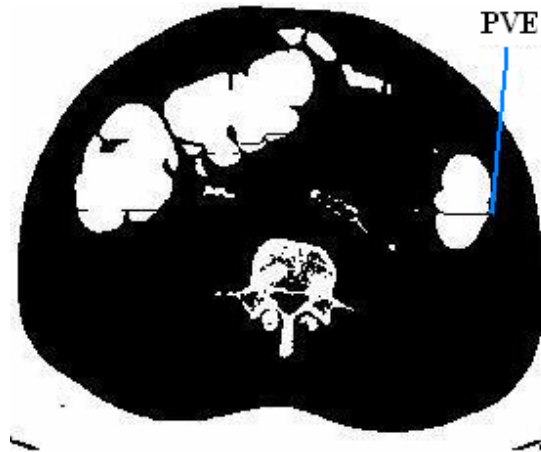
Figure 4.7 Partial volume effect between colon air and colon fluid (238th slice)

The problem can be solved based on the feature of the CT colon image. Because of gravity, the fluid gathers into some concave area of the colon, and the surface of the fluid remains horizontal. As a result, the fluid residues always stay right below the bowel air regardless of the patient position (prone or supine). Therefore, we propose to search for gap between the two classes in the vertical direction. The height of the gap must be within a certain range. A large gap range will mistakenly include other tissues, while a small gap range will miss the right cases. From our empirical experiment, we set the gap range to be not more than three voxels. Once this gap is detected, the partial volume effect can then be removed.

After searching for partial volume voxels, regions correspond to colon air and fluid residues can be connected. However, in some cases the lung (similar intensity as colon air) and the bone (similar intensity as fluid) also satisfy the condition because they are very close to each other at some places (Fig. 4.8). This problem will be resolved using region growing, which is described in the next section.
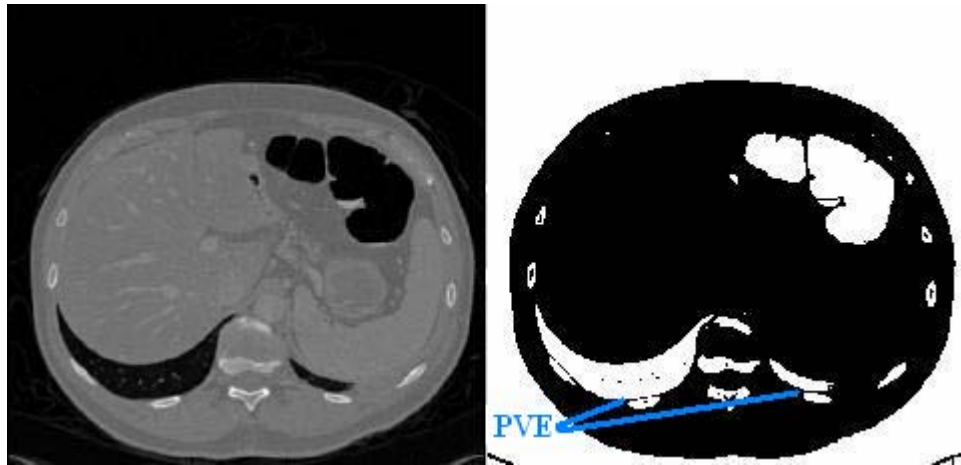
Figure 4.8 Partial volume effect between lungs and bone (88th slice)

4.2.3 Region Growing

Now that the colon air and fluid residues are segmented out, and the partial volume effect is removed, what remains is to extract the colon and eliminate other co-existing tissues like bone, lung and background. Region growing is an approach used to fulfill this task.

Region growing is a procedure that groups pixels into one region based on connectivity criteria. The diagram of 2D region growing is shown in Fig. 4.9. It normally starts with "seed" points, and expands the region by including the neighboring pixels (4 or 8-connected) that have similar properties with the seeds. The procedure continues in iterations until no pixels satisfy the similarity criteria. By this means, all the connected parts that have similar properties will be grouped into one region. 3D region growing can be easily achieved by extending the 2D neighborhood to 3D neighborhood.
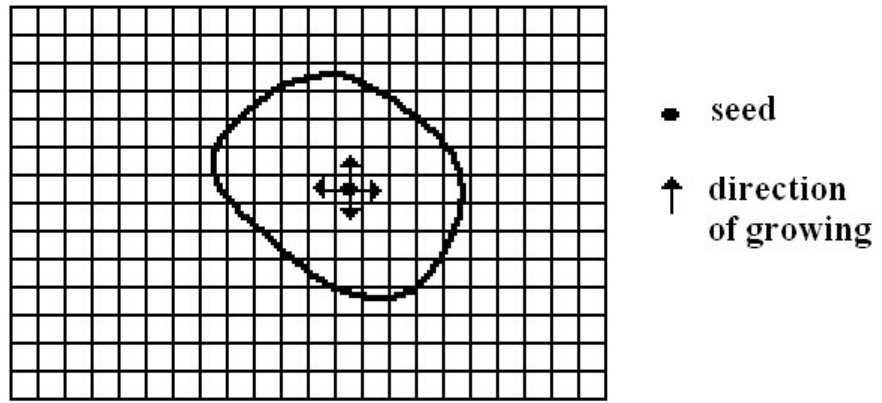
Figure 4.9 2D region growing

According to the rationale of the approach, the colon can be segmented out if the seed point is planted in the colon interior. The air in the lung, bone and background, are far from the colon and are not connected to each other, will not be extracted.

The selection of seed point is crucial here. Any voxel near the region of partial volume effect which belongs to the colon interior can be classified as the seed. However, as mentioned at the end of the previous section, another kind of PVE voxels exist between the lung and the bone. To automate this process without the need for user interaction, we try to differentiate these two situations. First, the surface of the fluid residues always remains horizontal, while the bone is not (Fig. 4.8). In addition, the maximum length of the connection area between colon gas and colon fluid is typically much larger than that between the lung and the bone. Based on these two conditions, we select a seed point by the criteria that it belongs to the PVE area with the longest horizontal length.

After seed point selection, 26-connected neighbors of the seed are examined to determine if they belong to colon based on their intensity similarity. When new voxels are added to colon, their neighbors are also examined in the same way. The process

repeats until no colorectal interior voxel is found. PVE removal ensures the connectivity of the colon air and colon fluid. On the other hand, the lung, bones and background are not connected with colon, so that these are not extracted as colon. As a result, only the colon is extracted.

Finally, opening is applied to remove noise, and the dataset is resampled to obtain an isotropic volume for later processing. Some examples of the result will be shown in the result section of this chapter.

4.3 Surface Rendering

After segmentation, the original CT grayscale images are converted into a binary 3D volume, in which the colon is the object and the others are all zeros. To visualize such 3D data, surface rendering is used. It aims to extract the iso-surface from the dataset by thresholding for each voxel. A triangle-based model is generated and then rendered.

The most common algorithm is marching cubes, which decides if a surface passes through an element and finally generates a triangular mesh. However for our case, the final model consists of a huge number of triangles, which cannot provide real-time navigation. Therefore, another algorithm that produces much fewer triangles is used here.

The algorithm known as "adaptive skeleton climbing" is proposed by Poston et al. [53]. It is based on marching cubes. The algorithm constructs boxes adaptive to local geometric surface by climbing from vertices to edges to faces. The boxes are bigger in

smooth regions so that bigger triangles are extracted. Therefore, the total number of triangles can be quite small, and real-time navigation is possible. Since it is not the focus of this project, we just give a brief introduction here. The details of the algorithm can be referred to Poston et al. [53] and Yeo's thesis [51].

4.4 Results

Finally, a binary volume dataset and a 3D VRML (virtual reality modeling language) model are generated. The former is prerequisite for subsequent sections, while the latter is for 3D visualization. We have obtained two datasets from NUH and the results are as follows.

4.4.1 Training Dataset 1

The first volume is a 512x512x471 supine CT dataset, with the in-plane resolution (distance between adjacent pixels in the 2D slice) of 0.67mm and the through plane resolution (distance between adjacent slices) of 1mm. The images in the previous sections of this chapter are all from this dataset.

The 88th axial CT image contains partial lungs and transverse colon, which is shown in Fig. 4.10(a). The partial volume effect after thresholding and the co-existence of extra-colonic tissues are depicted in section 4.2.2 (Fig. 4.8). The segmented slice is shown in the Fig. 4.10(b). From the figure, it shows that the colon air and fluid are connected. Further, the lungs are successfully removed, and only the colon is extracted.

(a)   **(b)**
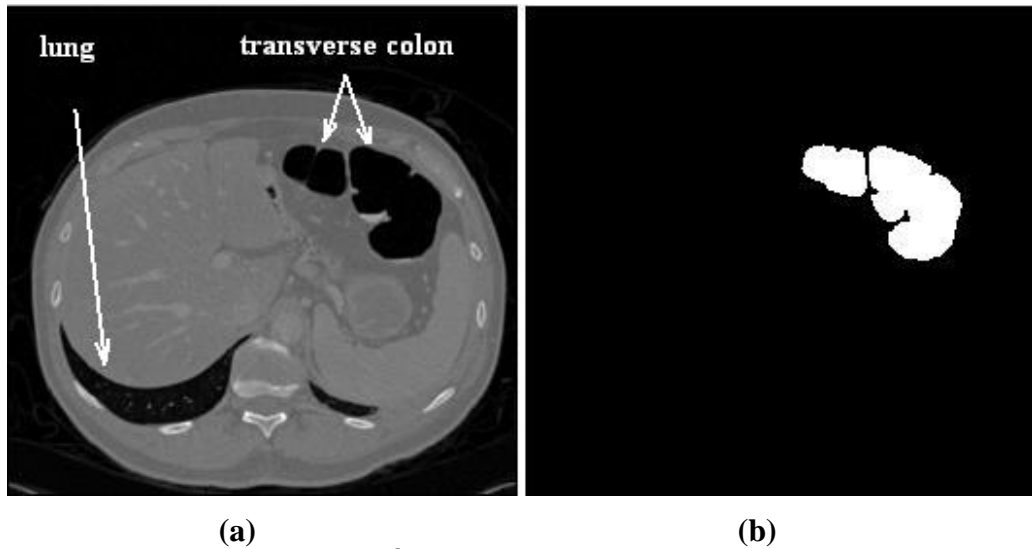
Figure 4.10 (a) The 88th axial CT image, (b) its segmented result

Fig. 4.11 shows the 238th CT image together with its segmentation result. This slice contains cross sections of the ascending colon, transverse colon and descending colon. The original image is superimposed with its segmented result, with the contour highlighted. As observed from the two images, partial volume effect is removed. In addition, some splitting parts, which are suspected to be the small intestine, are also eliminated.

(a)   **(b)**
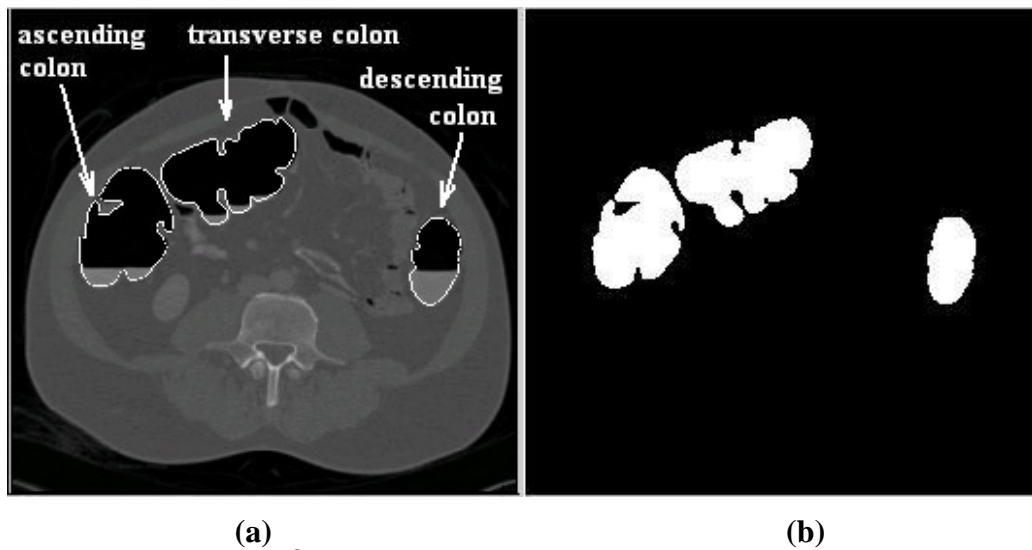
Figure 4.11 (a) The 238th axial CT image with segmented contour superimposed, (b) its segmented result

In Fig. 4.12, the reconstructed 3D model of the colon is shown. The cecum, ascending colon, transverse colon, descending colon and sigmoid colon are successfully segmented out through our algorithm. There is no rectum because the patient is not well prepared.
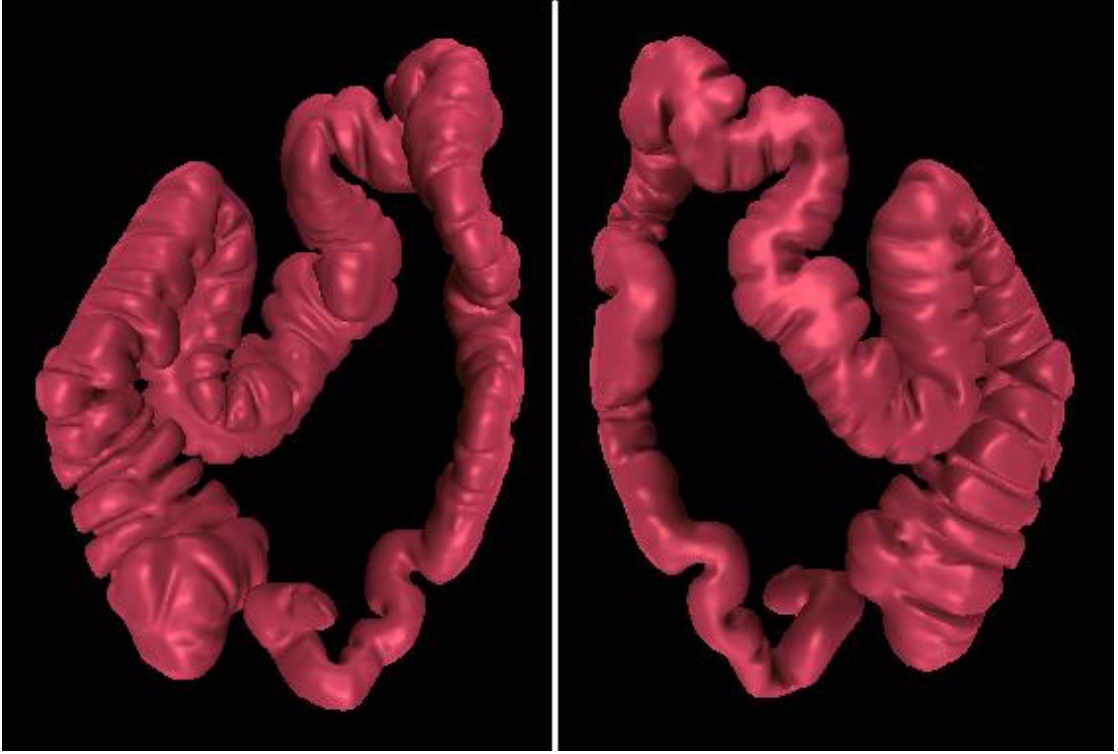
Figure 4.12 3D reconstruction of colon 1: front side (left) and back side (right)

4.4.2 Training Dataset 2

To further test our algorithm, a second volumetric CT dataset undergoes the same segmentation process. Its size is 512x512x438, and the intra-slice and inter-slice resolution are 0.7mm and 1mm, respectively. For this dataset, the patient is in prone position, so that the axial image is upside down as compared with that of the first dataset.

Fig. 4.13 shows two CT slices and their segmentation results. One original image is superimposed with the contour of its segmented image as shown in Fig. 4.13(c). As

seen, a good segmentation result is obtained. The colon is extracted successfully.
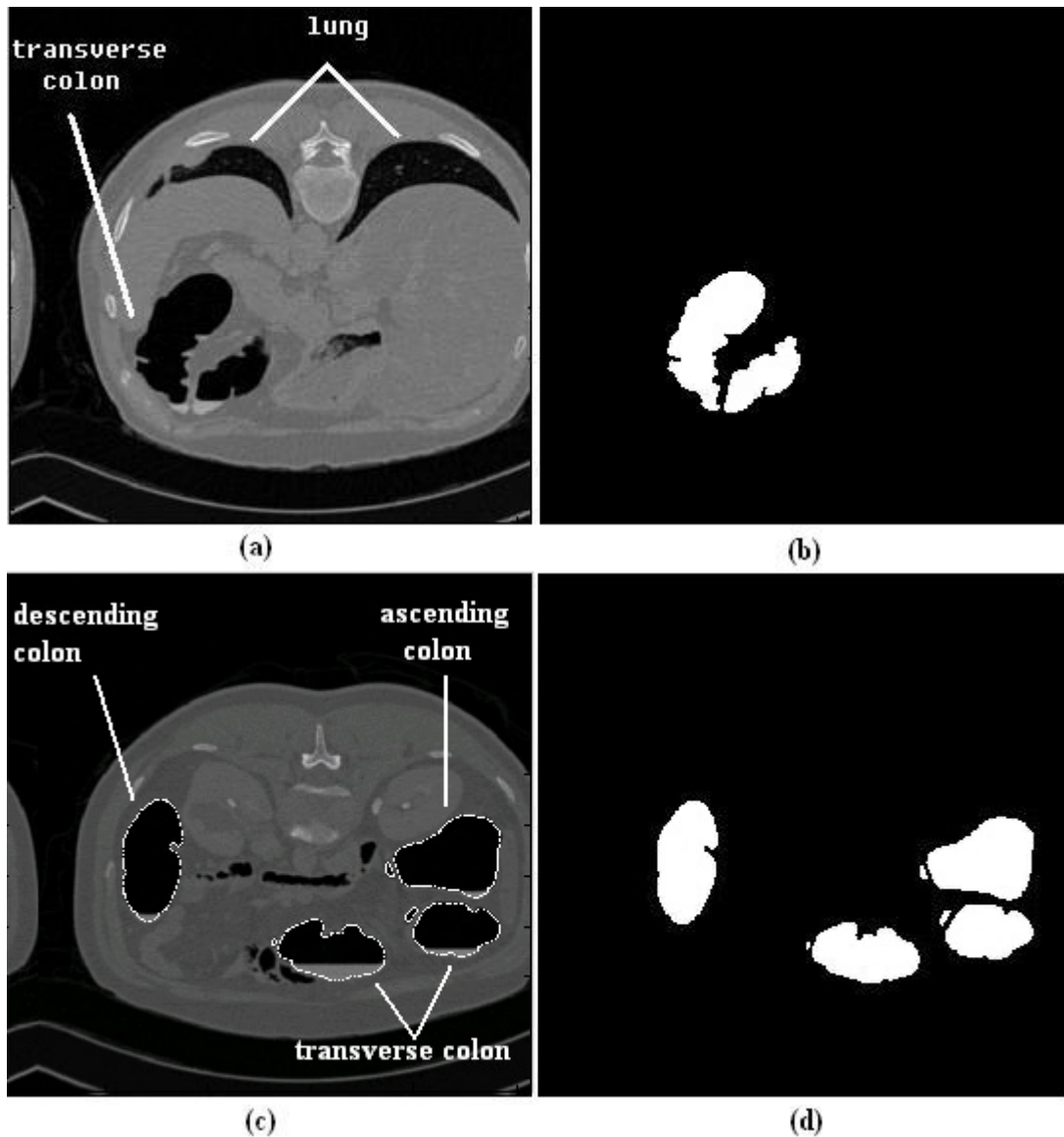
Figure 4.13 (a) The 56th axial CT image, (b) segmented result of (a), (c) the 139th axial CT image with segmented contour superimposed, (d) segmented result of (c)

A cross section of rectum is shown in Fig. 4.14, which does not exist in the first training data. A 3D view of the rectum is provided in Fig. 4.15. It is evident that the images of the first dataset are not well acquired. This second dataset is better, but is still not optimal. As seen from the 3D model in Fig. 4.15, the colon suddenly narrows around the sigmoid colon area. This is caused by suboptimal patient preparation and CT imaging.
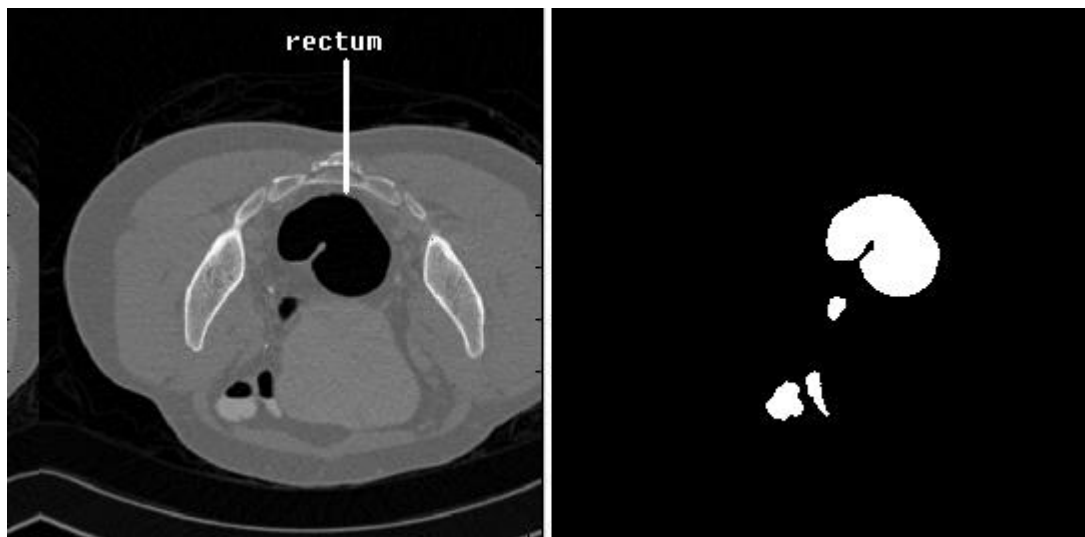
Figure 4.14 (a) The 336th axial CT image, (b) its segmented result

Figure 4.15 3D reconstruction of colon 2: front side (left) and back side (right)

The segmentation algorithm is shown to be effective and robust. Colon gas and fluid residues can be extracted as a connected object. Furthermore, all the background and extra-colonic tissues are eliminated. Finally, the colon body is obtained, which is needed for the subsequent modules.

<div align="right">

CHAPTER

5

</div>

Medial Axis Extraction

_____

This chapter describes the procedure for extracting the median axis of the colon. This axis is crucial for subsequent task such as fly-through or colon unfolding. The method of medial axis extraction is based on two forms of distance transform [41]. These transform will ensure that the axis is continuous and furthest away from colon surface.

5.1 Distance Transform

In this section, we will touch on two different distance transforms, distance from the boundary (DFB) and distance from the single seed (DFS). They differ in the initial selection of the seed set.

The distance transform works with binary 2D image or 3D volumetric data. It starts with a set of seeds, and calculates for each object voxel its minimal distance from the nearest seed. When the coding is done, every object voxel will be coded with a distance value, thus producing a distance field. The coding scheme depends on the

adopted distance metric.

The distance metric is defined according to the values assigned to the face-connected (orthogonal), edge-connected (2D diagonal) and vertex-connected (3D diagonal) neighbors of the seed point. Fig 5.1 depicts the application of some popular distance metrics in 2D images: the $1-\sqrt{2}-\sqrt{3}$ Euclidean metric, the 1-2-3 metric and the 3-4-5 Chamfer metric. In 2D case, only face-connected and edge-connected neighbors exist, so the third component of the metric is not shown.

At first, the seed points are coded with a starting value, and the other voxels are initialized to be infinity. Each voxel that is a neighbor of the seed points is then assigned with a value according to the distance metric adopted. For example (in Fig. 5.1(c)), if the 1-2-3 metric is used, the orthogonal object neighbors and the diagonal object neighbors are assigned with 1 and 2 respectively when the starting value is set to 0. The neighbors of the newly coded voxels undergo the same process. Suppose an intermediate voxel has been assigned to be n, and then its orthogonal neighbors, 2D diagonal neighbors and 3D diagonal neighbors (all inside the object) are coded to be n+1, n+2 and n+3. Such a voxel propagation procedure repeats until specific stopping conditions are met.
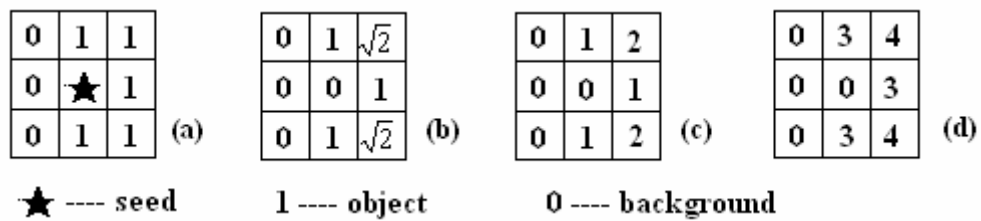
Figure 5.1 (a) Original image; distance transform with (b) $1-\sqrt{2}-\sqrt{3}$ **metric, (c) 1-2-3 metric and (d) 3-4-5 metric.**

The pseudo-code of the algorithm is outlined below:

Set the seed sets to be 1, object voxels to be ∞, and background voxels to be 0.
While distance transform (DT) change is true
{

 Set DT change to be false;
 For all the voxels in the seed set

 {

  For the 26 neighbors of the current seed

  {

   Compute the distance transform D_1 of its neighboring object voxel;

   Compute the minimal distance transform D_2 of this neighboring object voxel based on all of its neighboring seeds except the current seed;
   If $D_1 > D_2$

   {

    Set the distance transform of this object voxel to be D_2;

    Label this object voxel to be seed;

    Set the DT change to be true;

   }

   Else

    Set the distance transform of this object voxel to be D_1;

  }

 }

}

Next, the two different distance transforms are outlined:

(1) Distance Transform from the Boundary (DFB)

The boundary voxels of the object are selected as the initial seed points. As a result, the object voxels near the boundary are coded with small value, while the objects voxels in the center are coded with a large value. The later medial axis extraction makes use of this feature to ensure the axis is at the center. In order to improve computational efficiency, the 3-4-5 distance metric is chosen, which is a good approximation of the $1 - \sqrt{2} - \sqrt{3}$ Euclidean metric.

For this distance transform, the entire segmented dataset is coded with the shortest distance from the boundary. An axial cross-section of the 3D coded volume is shown in Fig. 5.2. As shown, the further an object voxel is from the boundary, the brighter (the larger distance value) it looks.
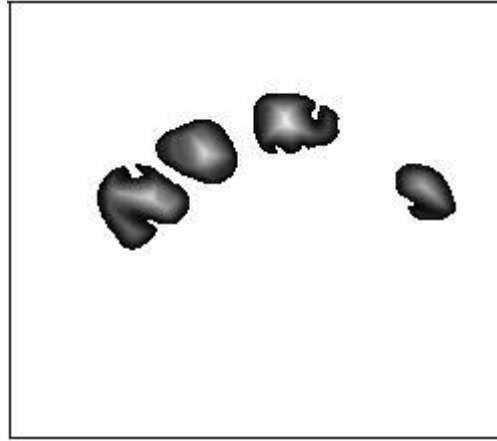
Figure 5.2 A cross-section of the 3D DFB map

(2) Distance Transform from the Single Seed (DFS)

In this distance transform, only a single point is selected as the starting seed. This point is also the starting point of the medial axis. Therefore, it is desired that it is located at either end of the colon. We propose to automatically select this starting seed based on the features of the colon morphology.

As shown in the 3D segmented colon model in section 4.4, the diameter of the colon is the largest at the cecum end, and then decreases when traveling along ascending colon, transverse colon and descending colon, finally increases slightly after arriving at the rectum end. Therefore, the voxel with the largest distance value from the boundary (DFB) will be located at the cecum portion of the colon. But this voxel is not at the end of the colon (Fig. 5.3(a)), so that it is not appropriate to be a starting seed. This voxel is

selected as the reference point, and then the colon dataset is coded with the DFS value in terms of this reference seed. As shown in Fig. 5.3(a), from the reference point to the other end of the object, the distance coded increases (the blue color represents the smallest value, and the red color represents the largest value). When reaching the other end, the voxel with maximum DFS value is located. This voxel can then be chosen as the best starting seed. The distance transform is applied again with respect to this starting seed, which produces the ultimate DFS field (Fig. 5.3(b)).

▲ reference point   ● starting seed

(a)   (b)
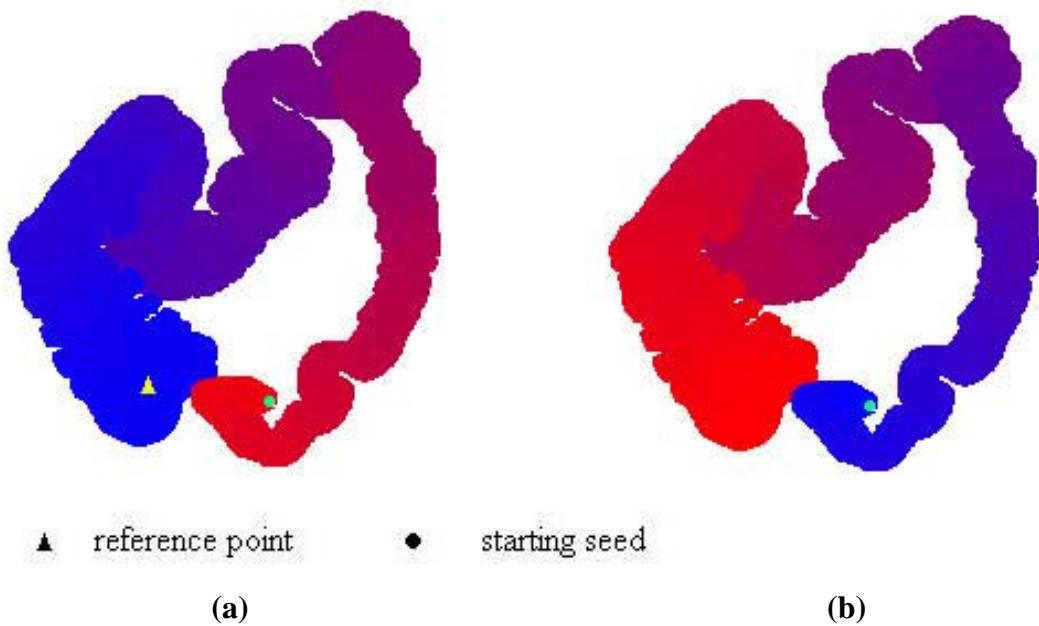
Figure 5.3 (a) DFS map with the reference point as the seed, (b) final DFS map in terms of the selected starting seed.

For fast computation, the 1-2-3 distance metric is used for DFS computation.

5.2 Axis Extraction

Now that two distinct maps are calculated, the DFS map is used to extract the shortest path, and the DFB map is to improve the centeredness of the path.

Since DFS map is generated using the 1-2-3 metric, the map can be divided into clusters with values from 1 to the maximum DFS value. Each cluster contains the object voxels with the same DFS value. Then the extraction process is divided into two phases:

(1) First, a path is extracted based on the principle of shortest path extraction (SPE) as shown in Fig. 5.4. The path starts with the object voxel p_1 with the maximum DFS value DFS_{max}. For the second voxel p_2 in the path, it is set to be one of the 6-connected neighbors of p_1, whose DFS value is the smallest among them. Since the 1-2-3 metric is used for DFS map, the DFS value of p_2 is $DFS_{max} - 1$, just one smaller than that of p_1. The same procedure repeats until the voxel with $DFS = 1$ is found. Thus, the extracted path consists of connected voxels with DFS value from 1 to DFS_{max}.
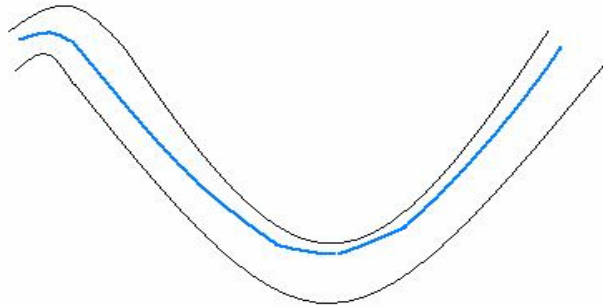
Figure 5.4 The shortest path hugging the corner at high curvature area

(2) The above obtained path is an axis connecting the two ends of the colon object. However, it tends to hug the corner at high curvature areas because it is the shortest path connecting two end points (Fig. 5.4). The DFB field is used to solve this problem. From each cluster, a voxel with maximum DFB value in the cluster is picked out. Such a voxel is called the medial point of this cluster, which is

supposed to be located in the center of the colon due to its high distance value from the boundary. Then except for the starting seed, every point in the path is substituted by the medial point in the corresponding cluster. If there is more than one medial point in a cluster, the one closest to the preceding point in the path is selected. As a result, the path is pushed to the center of the object. But this also leads to a discontinuity of the axis at the place of sharp bending, as shown in Fig. 5.5(b).

(a)   (b)
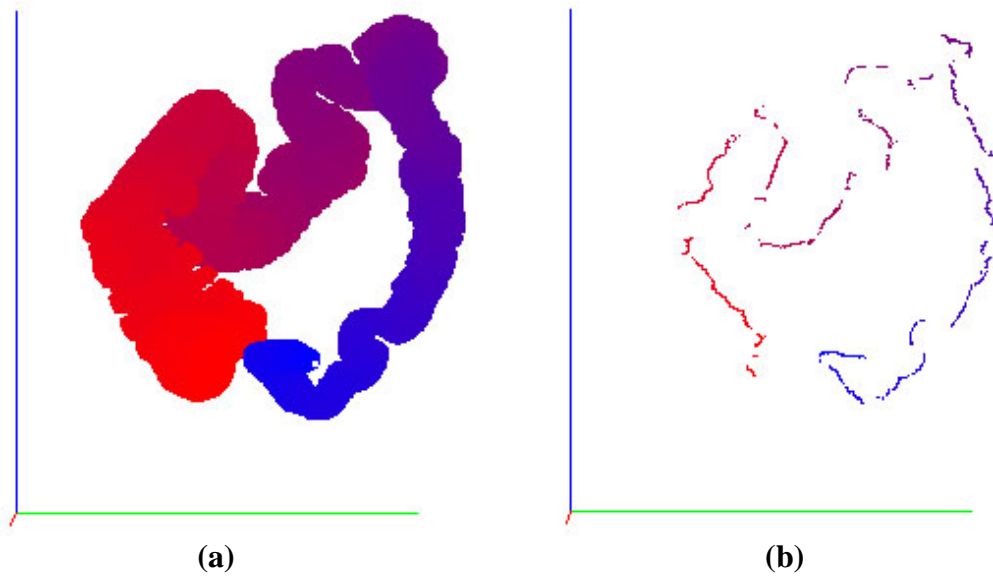
Figure 5.5 (a) DFS map of the colon, (b) initial medial axis corresponding to (a)

5.3 Axis Refinement and Connection

As stated above, the axis becomes discontinuous after replacement of the path points by medial point of discrete clusters. In this section, we present a method to refine and re-connect the axis.

From Fig. 5.5(b), there are both large and small intervals between adjacent axial points. For small intervals, linear interpolation can be used to fill in the interval without much loss of centeredness; while for large intervals, directly connecting two adjacent points

will either deviate a lot from the center, or even penetrate through the object surface.

Therefore, at the large intervals the axis is refined by using the local distance transform. Suppose the two ends of the interval are point p_i and p_{i+1}, a local distance transform is generated from p_{i+1} to p_i, with p_{i+1} chosen as the starting seed. Then a path is extracted from p_i to p_{i+1}, which could be inserted into the interval between p_i and p_{i+1}. The procedure is similar to that described in the previous section which extracts a centered path between two end points. Finally the large intervals are removed and the path is connected. In some cases when the object shape is too complicated, the inserted path may still be discontinuous. However, these discontinuities are of small intervals, which can be easily solved by interpolation.

After refinement above, the axis is continuous (Fig. 5.6(a)). However, this path is not one-voxel wide. Shortest path extraction is again applied to extract a one-voxel wide path and remove redundant points. Finally, a connected, centered and single-voxel wide axis is obtained (Fig. 5.6(b)).

<center>(a)   (b)</center>
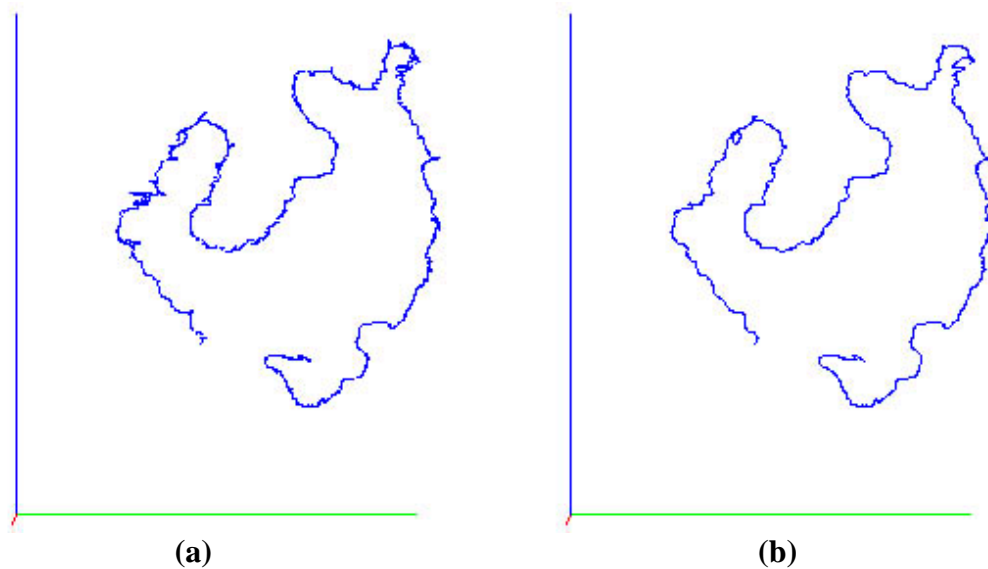
Figure 5.6 (a) Axis after refinement and connection, (b) one-voxel wide axis

5.4 Smoothness

The medial axis acquired up to the last stage is a centerline affected by the colon shape. Since the colon surface is curvy and complicated, the corresponding axis is jagged. For the fly-through navigation, such an axis will lead to a jerky movement of the camera. Moreover, the unfolding process requires a smooth axis to better avoid the frequent intersection of adjacent cross-sections of the surface. Therefore, the axis needs to be smoothed.

B-spline interpolation is applied, which balances the requirements of preserving the detail and smoothing the curve. Each four consecutive control points (picked out from the axis) define a segment of cubic curve. Thus, the interpolation is implemented segment by segment, resulting in a piecewise curve. Each segment is connected smoothly at the joint point as the B-spline curve is C^2 continuous.

Suppose the four control points is represented as $P^T = [P_0 \quad P_1 \quad P_2 \quad P_3]$, then the interpolated curve is:

$$C(t) = N(t)P^T \qquad (5.1)$$

where $N(t) = \dfrac{1}{6} \begin{bmatrix} (1-t)^3 \\ 3t^3 - 6t^2 + 4 \\ -3t^3 + 3t^2 + 3t + 1 \\ t^3 \end{bmatrix}$.

$N(t)$ is the basic function of B-spline curve. t is a real number between 0 and 1 representing the internal interpolated knots in the segment. At the start point of the segment $t = 0$, and at the end $t = 1$.

The advantage of this method is that each control point only has local influence, which better approximates the local shape of the curve. The smoothed medial axis is presented in Fig. 5.7.
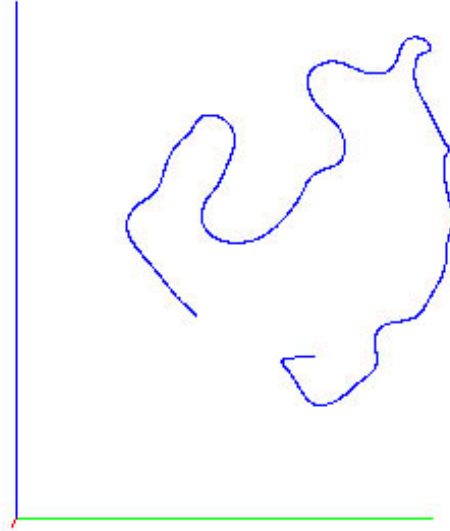
Figure 5.7 The final medial axis after smoothing

5.5 Results

Besides the two CT datasets used in the segmentation stage, we created a synthetic colon to validate the algorithm of the medial axis extraction. The results for three datasets are presented respectively.

5.5.1 Synthetic Model

The synthetic model is a hollow tube, whose surface is much smoother compared to that of the real colon. Unlike the real colon, the diameter of the tube changes gradually, which provides a good platform to test the algorithm. The size of the dataset is 512x512x300.

As shown in Fig. 5.8, the medial axis is in the center of the tube in the form of a black curve. Combined with visual inspection in fly-through navigation, the axis we obtained is highly centered and satisfactory.

(a)   (b)
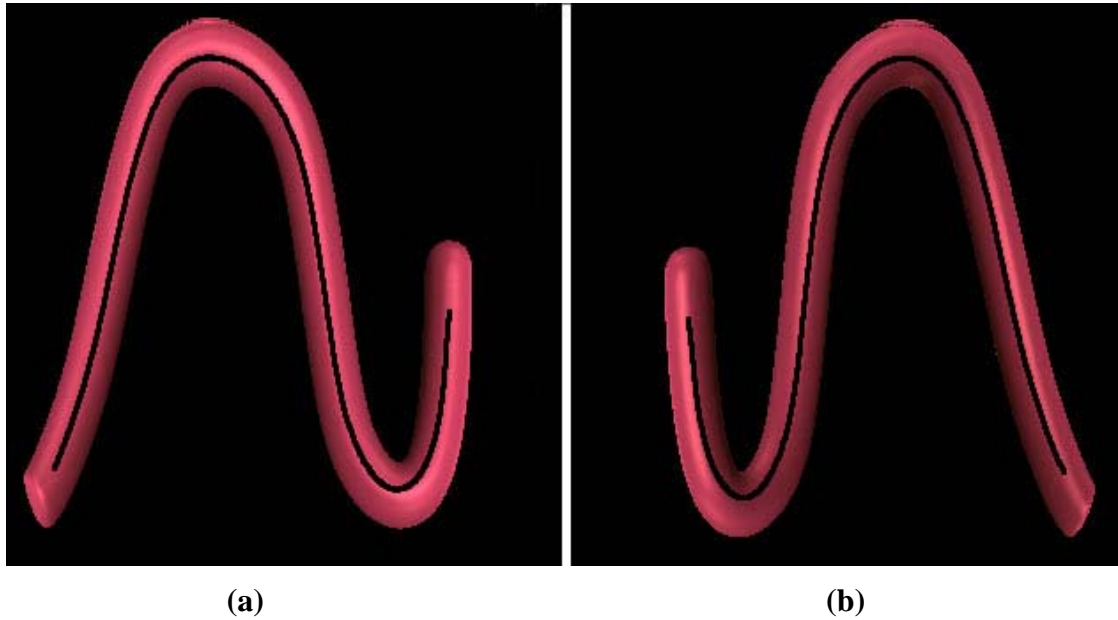
Fig 5.8 Synthetic model with the medial axis (a) front side, (b) back side

An axial cross-section is taken at a specific position of the model (Fig. 5.9(a)). The corresponding 2D slice is shown in Fig. 5.9(b), where the white circles represent the intersections between the tube and the slicing plane. The points in the middle of the circles are the intersection of the extracted median axis and the slicing plane.
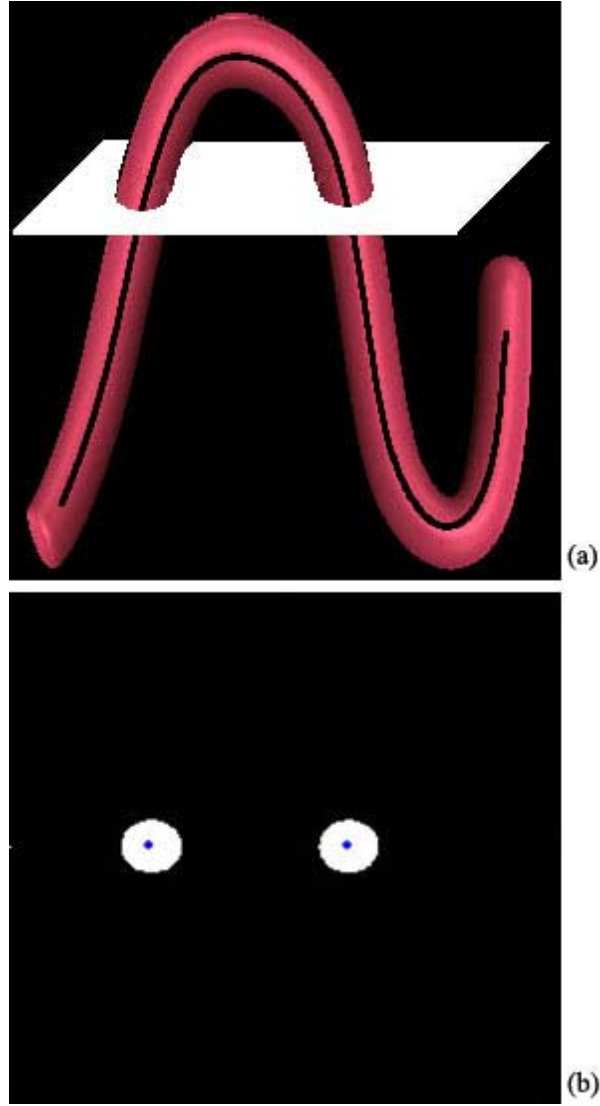
Figure 5.9 (a) 3D model intersected with a plane, (b) corresponding cross-section (200th slice)

5.5.2 Training Dataset 1

This dataset is the same as that used in the segmentation process. However, the segmented dataset is resampled to be 512x512x702 in order to obtain an isotropic volume data.

In Fig. 5.10 the extracted centerline is displayed inside the colon model as a white curve (black dots along the curve represent control points in B-spline interpolation as introduced in section 5.4). The centeredness of this centerline is proven through fly-through navigation and the high distance value of the axial points from the colon surface. A 2D cross-section is depicted in Fig. 5.11, where the path points are also highlighted.
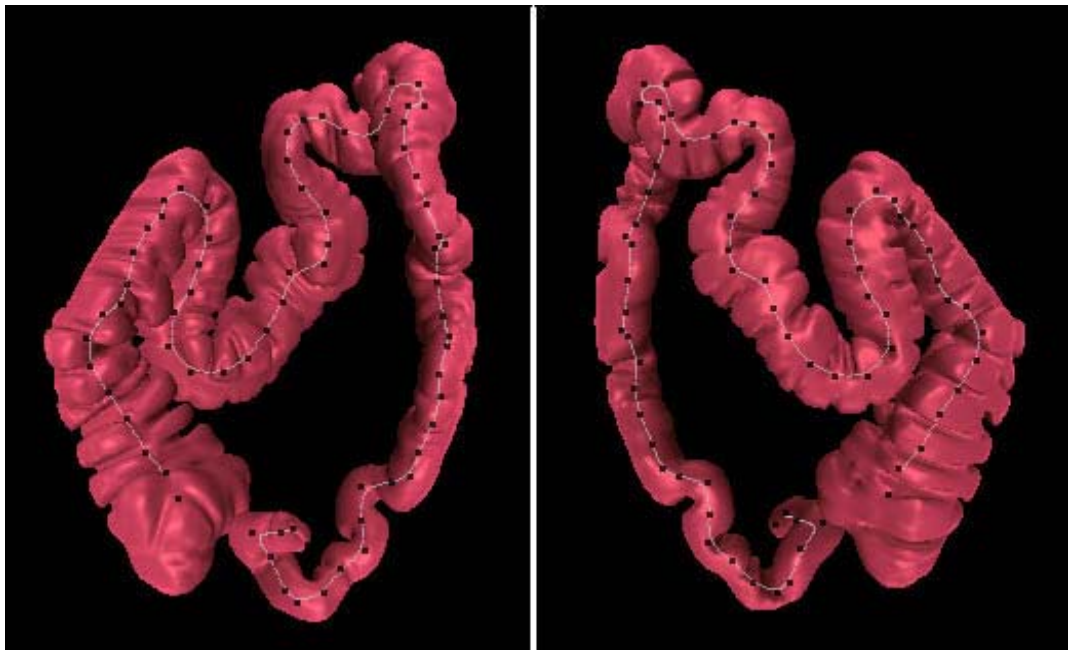
Figure 5.10 Colon 1 with medial axis: (a) front side, (b) back side
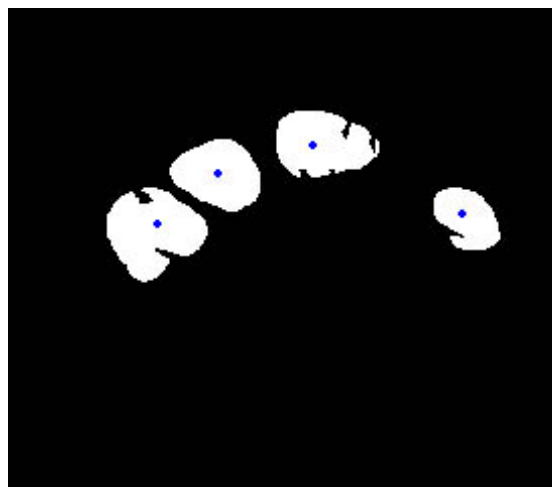
Fig 5.11 2D axial cross-section with axial points designated (404th slice)

5.5.3 Training Dataset 2

Colon dataset 2 was also resampled to form a 512x512x625 isotropic volume. From Fig. 5.12 and 5.13, the obtained medial axis is located in the center of the colon body, which provides a satisfactory flying path for endoluminal navigation.
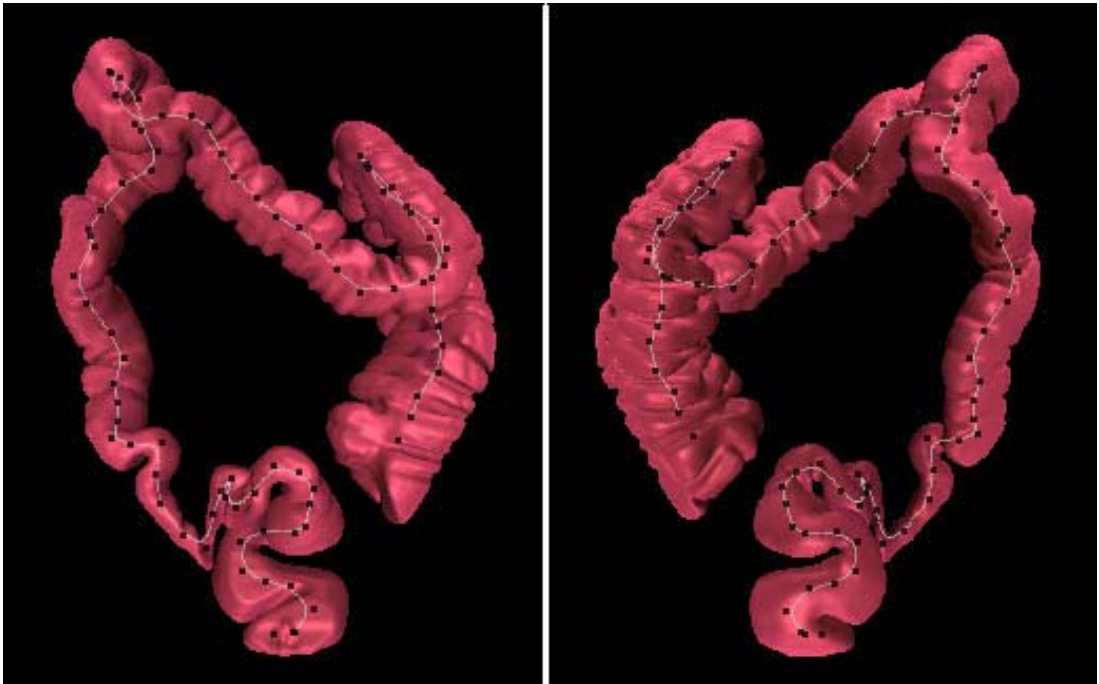
Figure 5.12 Colon 2 with medial axis (a) front side, (b) back side
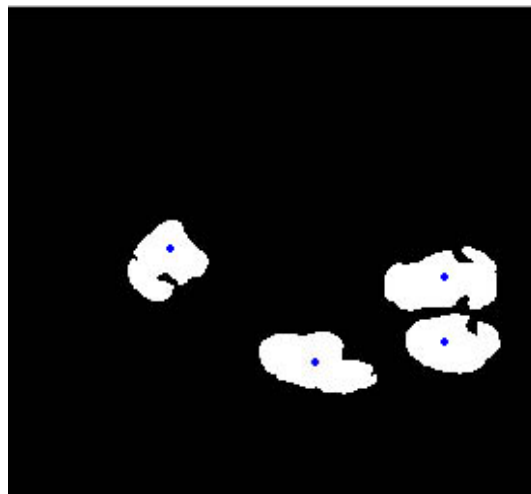
Figure 5.13 2D axial cross-section with axial points designated (447th slice)

The resultant median axes extracted from the three datasets are test through fly-through navigation. The real time fly-through navigations show that the extracted axes are all well centered and smooth.

The program for medial axis extraction is executed on a Pentium Ⅳ 2.4GHz machine. For training dataset 1 (512x512x702) and training dataset 2 (512x512x625), the computation time is 11.43 minutes and 13.03 minutes, respectively. The training dataset 2 has a longer axis, so the processing time is longer. In total, the calculation time is acceptable for clinical use.

CHAPTER

6

Colon Unfolding

_____

As explained in chapter 2, the endoluminal view of the colon suffers from coverage deficiency of the inner surface, especially for areas behind the folds. Therefore, we propose to develop a procedure to extract the unfolded view of the colon for better polyp detection. This process virtually dissects and flattens the colon wall to provide a complete view of the colon surface. In this section, the algorithm for colon surface unfolding is presented.

6.1 Method Overview

The straightforward way of unfolding a tube like object is to obtain cross-sections perpendicular to the centerline slice by slice along its longitudinal direction (Fig. 6.1). Then the series of cross-section are aligned and stacked in longitudinal order to "straighten" the object. Finally the cross-sections are "opened" in the latitudinal direction, thus generating a straightened and flattened surface. Fig. 6.1 illustrates a simple example where the object is a simple cylinder. In this case, cross-sections are

parallel to each other, and thus no straightening is needed. The circular cross-sections are stretched to lines, all of which constitute the final flattened surface, a rectangle in this case.
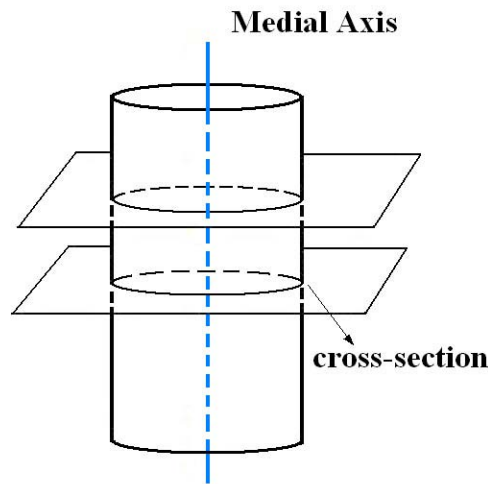
Figure 6.1 Parallel cross-sections of cylinder

However, when the object is the colon, in which the tube is curved with sharp bending and the surface is rough, the situation becomes complicated. At high curvature areas where the surface is usually undulated, cross-sections tend to intersect as illustrated in Fig. 6.2. In this situation, the region where the intersection happens will be sampled several times, i.e., the same region will be included in several different cross-sections. As a result, if there is a polyp in this region, it will be visualized repeatedly on the unfolded surface. This will cause false positives in polyp detection. In addition, if the curvature is extremely high, the order of the cross-sections will be greatly disturbed by excessive intersection, thus yielding a surface that loses its real shape. Therefore, the straightforward planar cross-section cannot satisfy this sophisticated situation. A method that could acquire curved cross-sections adaptive to local curvature is desired.
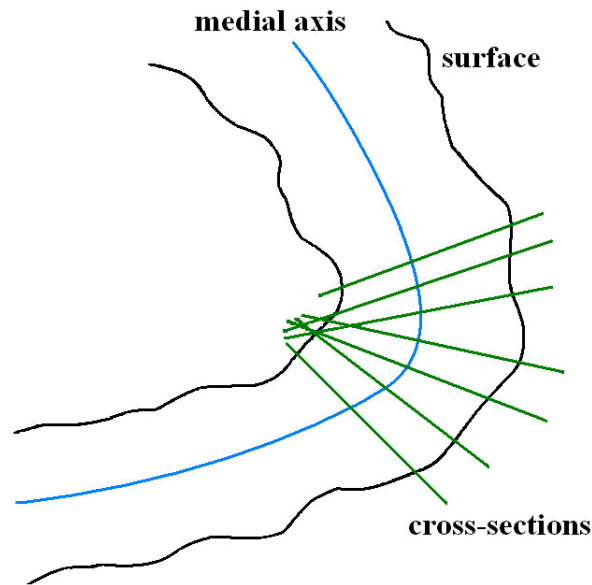
Figure 6.2 Intersection of cross-sections at high curvature area

The algorithm to calculate curved cross-sections is based on the gradient field of distance map in the object [50]. By computing for each object point its distance value from the nearest centerline point, a distance map can be generated. Then for each cross-section, several rays are cast from the medial axis along the gradient direction of the distance map. The surface samples hit by the rays constitute the final curved cross-sections. Since the rays are traced in the gradient vector field, cross-sections will not intersect with each other.

After curved cross-sections are obtained, the contour may not be closed due to obstacles of sophisticated surface. We further refine the cross-sections by the snake algorithm based on two kinds of distance energy functions, thus complementing and fitting the contours to the local surface.

To "open" the curved section consistently, we computed an anchor axis that is approximately parallel to the medial axis along the surface of the colon. This anchor

axis is a reference for aligning the cross-sections longitudinally and for opening the cross-sections latitudinally. Finally, the sampled surface is projected to 2D grids, forming the unfolded surface of the colon.

The process of the algorithm will be elaborated on in the next few sections (refer to Fig. 3.2 for the flowchart).

6.2 Procurement of Cross-sections

As in the previous section, the key point in the unfolding process is to compute "good" cross-sections. The procedure to calculate cross-sections comprises two portions: distance map and ray casting.

6.2.1 Distance Map

In chapter 5, we presented the algorithm for two different forms of distance transform: distance transform from the boundary and the distance transform from a single seed. In fact, they differ in two aspects: the starting seed set and the distance metric.

In this section, since a highly accurate gradient vector is required, the $1-\sqrt{2}-\sqrt{3}$ Euclidean distance metric is chosen. Here, the starting seed set is selected to be the medial axis obtained from the previous chapter. With these two conditions, the distance transform algorithm is computed on the segmented volume data using the procedure as presented in section 5.1. As a result, the resultant Euclidean distance map is a volume data in which every object voxel is endowed with a value of minimum distance from the medial axis of the colon. The voxels outside the colon are not processed as these

are irrelevant. Therefore, the object points near to the central path are coded with low value, while the surface points are coded with high value. Contrary to Fig. 5.2 (distance transform from the boundary), the center is dark, while the boundary is bright (Fig. 6.3).
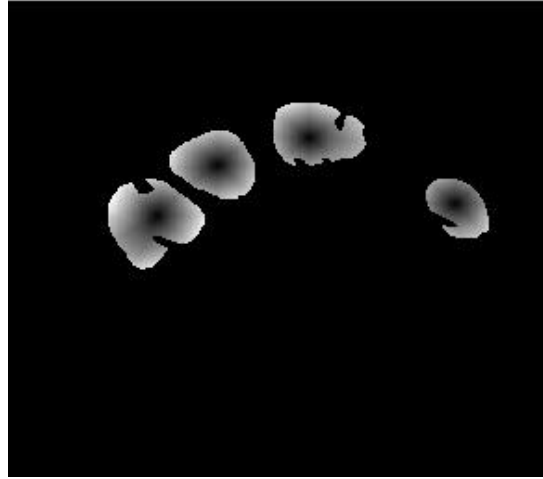
Figure 6.3 A cross-section of 3D distance map from the medial axis

Cross-section extraction is a crucial step in the unfolding process. In order to ensure precise ray casting, we perform tri-linear interpolation (Appendix A) on the discrete dataset to improve the resolution of the computed gradient.

6.2.2 Ray Casting

As explained in section 6.1, the planar cross-sections perpendicular to the central path is not satisfactory. Here, we aim to obtain curved cross-sections that are adaptive to local curvature.

For unfolding, at any point in the median axis (as in Fig. 6.4), we would need to compute the corresponding surface contour. A number of rays following the radial directions are cast out from the point on the median axis of the colon, and they are

traced toward the colon surface inside the colon. All the surface samples hit by the rays make up the cross-section at this path position. For every position in the medial axis, a cross-section can be obtained using this procedure.
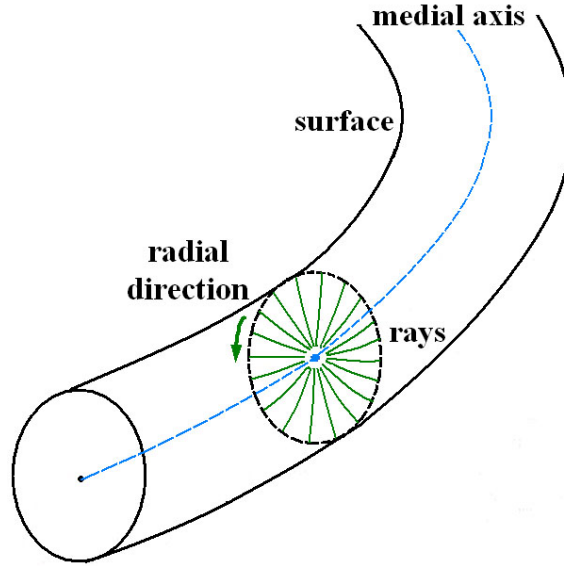
Figure 6.4 Ray casting at one path point

For each cross-section, the rays are cast at constant interval of 5 degrees along the radial direction (Fig. 6.4), e.g., 0°, 5°, 10°, … , 355°. The starting direction of every ray is selected to be in the plane perpendicular to the central path. These starting points form a small circle centered at the path point.

The key is how to propagate the rays to reach the surface. When rays are guided in the direction orthogonal to the central path, the obtained cross-sections are planar, which will cause neighboring intersection at high curvature regions as previously mentioned. Instead, if rays are led in the gradient direction of the Euclidean distance map generated in the last section, the rays remain perpendicular initially but will turn with increased curvature. This can be explained by the fact that the gradient direction represents the direction with the maximum change of distance value, i.e., the direction for a ray to reach the surface in the shortest path. Tracing the rays in this direction will

not lead to ray intersection. Accordingly, each ray goes outward step by step until it arrives at the colon surface.

As a result, the series of cross-sections are curved avoiding intersections, and well ordered along the central path. Contrary to the planar cross-sections in Fig. 6.2, the curved cross-sections are displayed in Fig. 6.5.
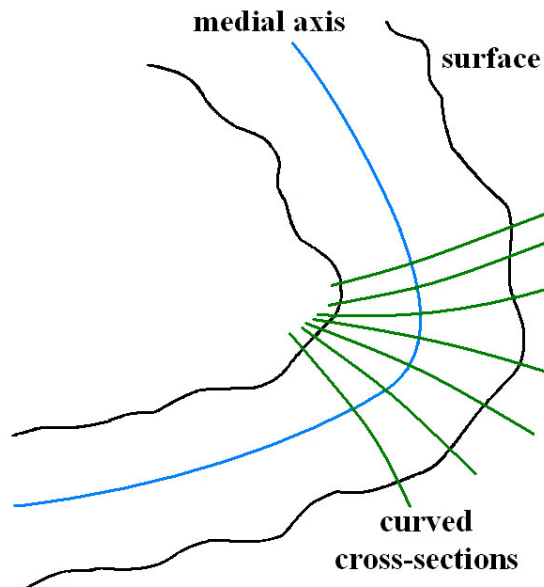
Figure 6.5 Curved cross-sections without intersection

6.3 Refinement of Cross-sections

Since a certain number of rays are cast for each cross-section, the same number of surface samples is obtained. In practice, this number can be set with a large value so as to densely sample the colon surface. However, this is typically not sufficient to extract the full surface contour.

When the curvature of the cross-section changes gradually, the ray casting would be able to obtain sufficient surface samples for reconstruction. As shown in Fig. 6.6, the

obtained contour is closed, and the distance of the surface points from the center changes gradually.
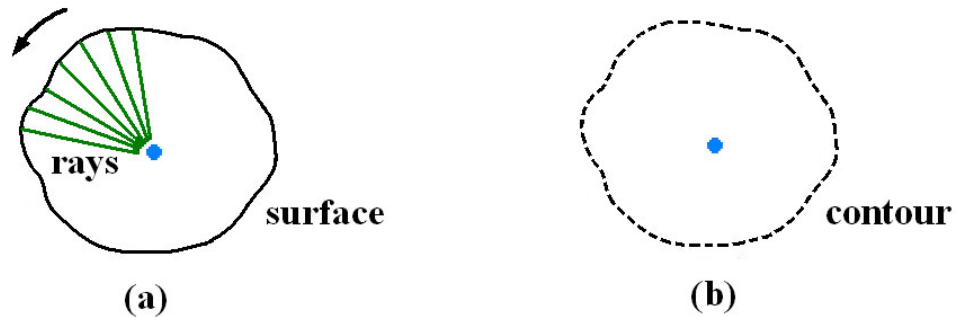
Figure 6.6 Sketch map of (a) ray casting in smooth area, (b) obtained closed contour

In the situation where the surface is rough, or a fold or polyp exists (Fig. 6.7(a)), the area where the curvature changes sharply (in red) cannot be fully reconstructed and the obtained contour is not closed. At the disconnected part of the contour, a large gap exists between adjacent contour points. As depicted by the red line in Fig. 6.7(b), simply increasing the number of the rays cannot solve the problem because some portion sticking out is out of the reach of the rays. Therefore, a snake algorithm is used to refine the extracted contours.
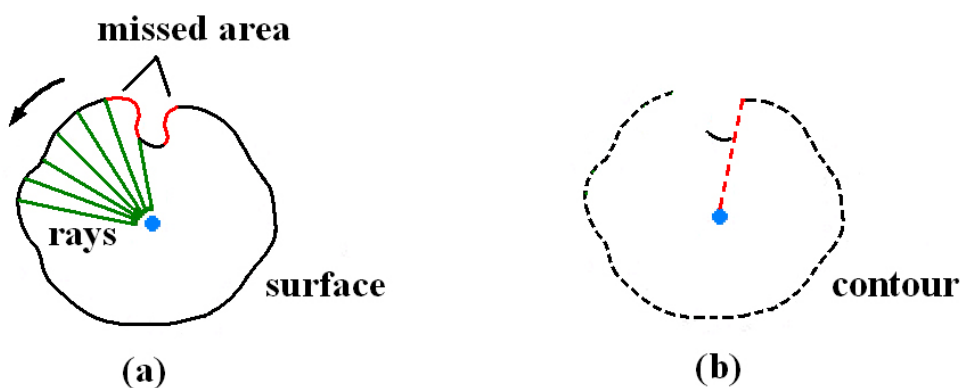
Figure 6.7 Sketch map of (a) ray casting in rough area, (b) obtained incomplete contour

The snake algorithm deforms the contour to match some features of interest in an image. The features are usually edges and object boundaries, especially in medical image processing.

An initial approximation of the boundary of the object should be given, and then an active contour model is used to find the optimal boundary. The active contour is an ordered collection of n points:

$$V = \{v_1, v_2 ... v_n\}$$

The points in the contour iteratively approach the object boundary by minimizing a chosen energy function E. For each point in the neighborhood of v_i, an energy term is computed:

$$E_i = \alpha E_{int}(v_i) + \beta E_{ext}(v_i) \tag{6.1}$$

$E_{int}(v_i)$ is an energy function dependent on the shape of the contour and $E_{ext}(v_i)$ is an energy function dependent on the image properties, such as the gradient near point v_i. α and β are constants providing the relative weighting of the energy terms. E_i, E_{int} and E_{ext} are matrices. The value at the center of each matrix corresponds to the contour energy at point v_i. Other values in the matrices correspond spatially to the energy at each point in the neighborhood of v_i.

Several forms of energy functions can be used for different cases. Here, for simplicity, $E_{int}(v_i)$ is not used because our purpose is to deform the contour based on the distance map, which will be elaborated below. We choose the negative gradient of the distance map as the energy function E_{ext}. Each element $e_{jk}(v_i)$ in the matrix $E_{ext}(v_i)$ is then defined as:

$$e_{jk}(v_i) = -\left|\nabla D(p_{jk}(v_i))\right| \tag{6.2}$$

p_{jk} is the point corresponding to $e_{jk}(v_i)$, and D is the value of distance map.

Each point, v_i, is moved to the point, v'_i, corresponding to the location of the minimum value in E_i. As in Fig. 6.8, v_i and its neighboring points all have a discrete energy value. v_i finally moves to the point v'_i which has the lowest energy value in its neighborhood. For all the points in the contour, the same procedure repeats until no more replacement of contour points occurs. If the energy functions are well chosen, the final contour will stop at the boundary of the object.
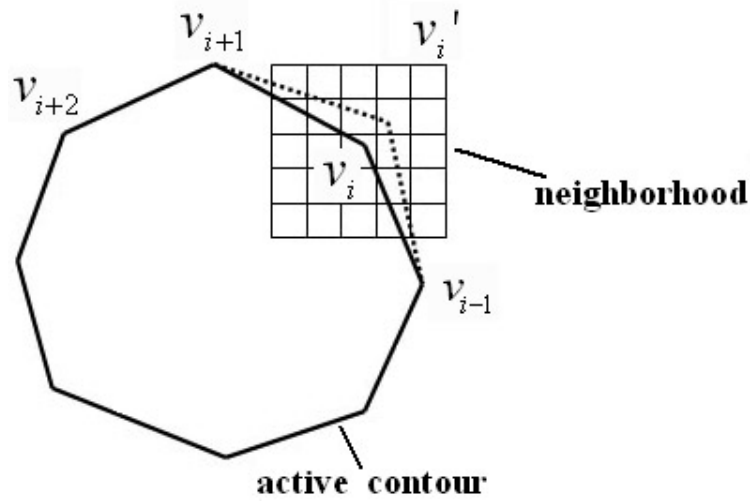
Figure 6.8 Movement of contour points by snake

For extracting the cross-section of a colon, two different energy functions are chosen.

(1) As shown in Fig. 6.9, when a large gap between adjacent contour point v_i and v_{i+2} is detected, a new point v_{i+1} is interpolated. Then the snake algorithm is applied to move v_{i+1} to the actual local boundary (drew in red). The energy function used here is selected to be the negative gradient of the Euclidean distance map from the medial axis (Eq. 6.2), because the area inside the contour is under the control of this distance map

in this situation without large convex protrusions.
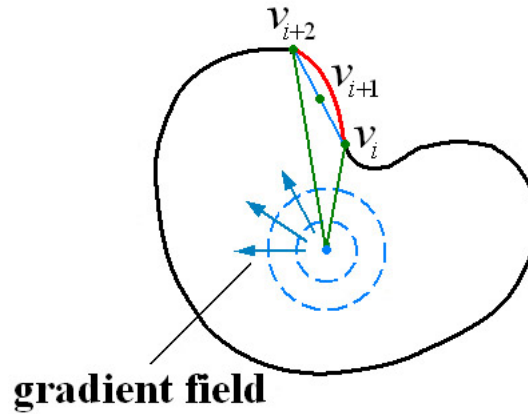
Figure 6.9 Sketch map of snake by distance map from the center

Since the distance value increases from the center to the boundary, the gradient direction points to the boundary. The region outside the object is also coded with the distance value from the center, but is set to be the negative value. Thus the gradient field outside the object also points to the object boundary. Therefore, with the energy function set to be negative gradient, active contour points can be directed to the surface in the shortest path by iteratively moving to the points with minimal energy. The procedure stops when the distance between adjacent points is sufficiently small.

(2) For the situation where there is a big convex portion in the cross section, the previous procedure cannot extract the full cross section successfully. For the case in Fig. 6.10(b), a point v_{i+1} is interpolated between the disconnected portion that ends with v_i and v_{i+2}. Based on the snake algorithm as described in the previous section, v_{i+1} will gradually approach v_{i+2} and finally stop at it.
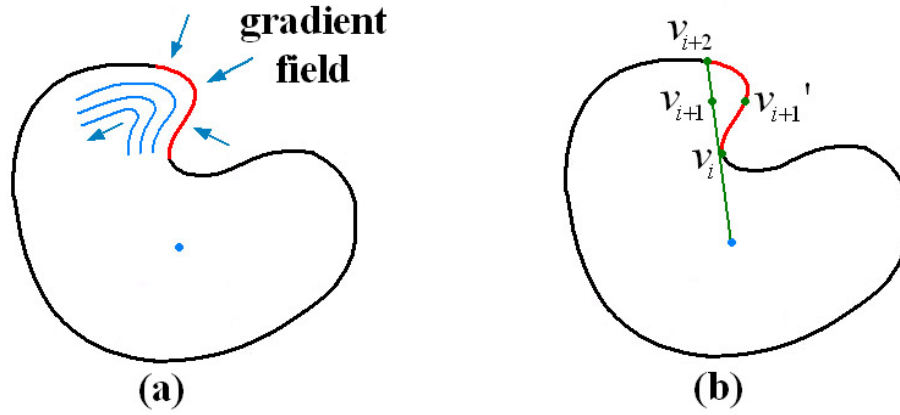
Figure 6.10 Sketch map of snake by distance map from the boundary

To tackle this problem, we propose to use the Euclidean distance map from the boundary. As shown in Fig. 6.10(a), this kind of distance map can generate a gradient field well matching the curvature of the convex portion (drew in red). By adopting the gradient of the distance map from the boundary as the energy function, v_{i+1} could successfully arrive at desired $v_{i+1}{}'$ which has the minimum energy as shown in Fig. 6.10(b).

Combining the above two snake algorithms, the full cross section, which is essential for unfolding, can be extracted.

6.4 Projection onto 2D Grids

The previous section has described the procedure to sample the colon surface through a series of curved cross-sections. This section will touch on unfolding of the cross-sections to form a planar view of the colon surface. A cross-section will be formed for every 1mm along the median axis. Each cross-section is used for sampling the distance of the surface from the median axis. The measurements from the

cross-section will be used to form the first horizontal line of the unfolded view. The following cross sections will be stacked in the vertical direction. Through this process, the 2D image for the unfolded colon surface is formed. Therefore, the surface is projected onto a 2D plane with the height illustrating the uneven inner surface.

First, we need to select a reference line along the colon surface, such that we can use it as the opening point for each cross section. It is selected to be a line approximately parallel to the medial axis, and lies along the surface (in Fig. 6.11).
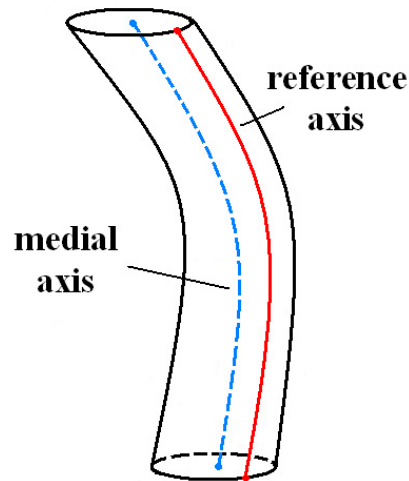
Figure 6.11 A reference axis for unfolding

Then the cross-sections can be projected onto 2D grids in terms of the reference axis. The projection is along x grid line and y grid line, respectively. Suppose the contour is unwrapped in the counterclockwise direction, then the reference axis corresponds to the 0 location in the x grid line, and the contour is spread along the x grid line. An example of the unfolded surface is shown in Fig. 6.12(a). The width is different along the vertical direction because of the various diameters along the colon. However, this view is not realistic for examination. Therefore, the reference axis is positioned in the center of the surface, and from left to right the contour points are mapped to the grid line accordingly (Fig. 6.12(b)). This surface is similar to real dissection.

<center>(a)   (b)</center>
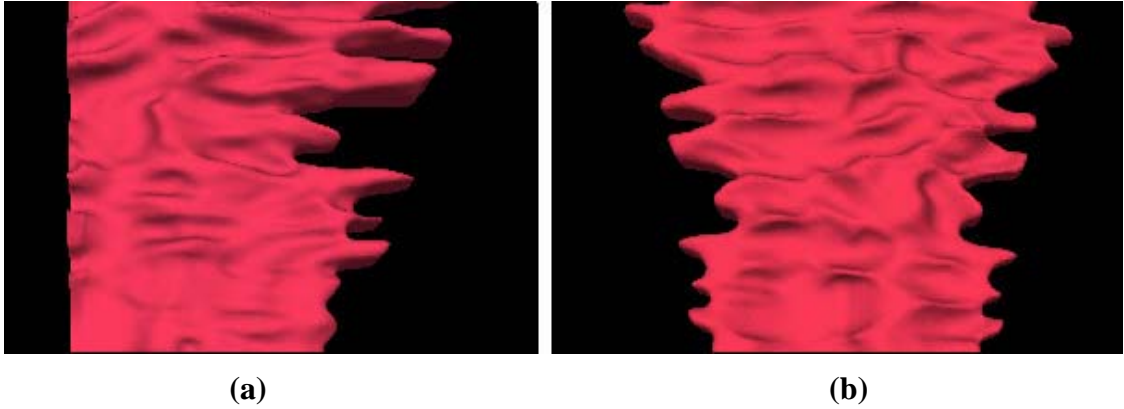
Figure 6.12 An example of unfolded surface (a) with reference axis in the left, (b) with reference axis in the center

In this situation, suppose the reference axis is at the $0°$ position of the contour, then the left and right edge of the unfolded surface, i.e., the cutting edge on the 3D object, is around $180°$ of the contour. The structures near the edge cannot be well examined. Directly duplicating the surface at the edge, i.e., copying a portion of one edge to be connected with the other edge, is not applicable. When the surface is rearranged with the reference axis at the center, all the other contour points are symmetrically distributed to the left and right side of the center. The curves at the two edges will be symmetrical, and therefore cannot match each other when connected together.

Here, to solve the problem at the edge, we propose to generate an opposite view to the above surface. For example in Fig. 6.13, when the reference axis is set at the $0°$, the cutting edge is around $180°$. So the surface is unwrapped for the second time, using the $180°$ reference axis. In this case, the cutting edge will be at $0°$. Therefore, the surface at the edge in the above surface is now at the center. By these two views, all the structures of the surface can be fully examined. The result will be further discussed in the next chapter.
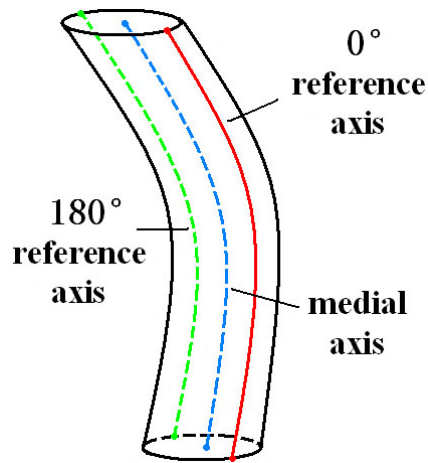
Figure 6.13 Two opposite reference axes

For every cross-section, the contour points are projected to the x grid line along radial direction, such as α_0, α_1, ... , α_n. The $0°$ point always corresponds to starting point indicated by the reference line. Then the contour points are mapped onto the x grid line. We have explored two different approaches for mapping contour points to the grid line. Fig. 6.14 gives a pictorial view on the typical approach of unfolding the colon surface. The mapping of the points sampled by adjacent rays is taken as constant in the grid line, i.e., the segment length between adjacent rays is set to be a constant distance l when projecting onto the grid line. The mapping is based on the angle of the ray. This results in a certain degree of distortion in the sense that the size of the "mapped" polyps depends significantly on the local radius of the colon. Therefore, the contour experiences a certain degree of deformation due to the unfolding.
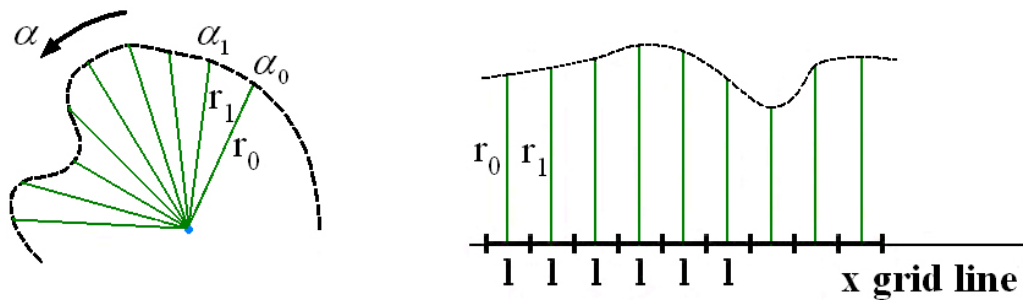
Figure 6.14 (a) One cross-section, (b) corresponding projection onto regular grid

We use another form projection which better preserves the actual length of each segment of the contour in 3D space. The distance between adjacent rays is approximated by the arc length. As illustrated in Fig. 6.15(a), α_0 is assumed to be 0 degree, so the angle between the first two rays is α_1. Then, l_1 is approximated by

$$l_1 = 2 * r_0 * \tan(\alpha_1) \tag{6.3}$$

For every segment on the contour, the same approximation is made and projected to the grid line (Fig. 6.15(b)). At the place where the radius of the contour is small, such as r_i and r_{i+1} corresponding to the rays at the degree of α_i and α_{i+1}, the segment length l_i and l_{i+1} becomes smaller when projected to the x grid line. Thus, the projected segment length l is adaptive to the local contour, better preserving the length of the local 3D shape.
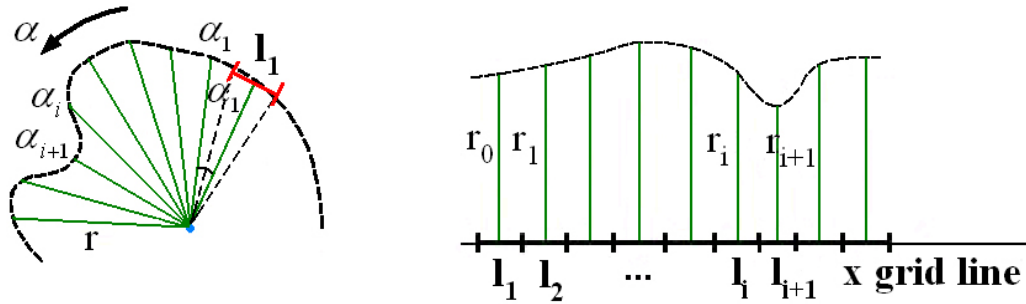
Figure 6.15 (a) One cross-section, (b) corresponding projection preserving the segment lengths

With each cross-section projected to the horizontal grid line, the 2D unfolded colon surface can be formed by stacking these "projected" lines in the y direction. The y-direction separation between adjacent "projected" cross section is approximated by the distance between the adjacent "seed" point on the median axis.

Directly transferring the height field to the 2D grids may not be a good display for the

colon surface. Suppose a polyp protrudes out from the colon wall, it is nearer to the medial axis compared with its surrounding area. Thus, the polyp is concave after projection because the height value of the polyp is smaller (Fig. 6.15). However, when a colon surface is unwrapped, polyps are desired to stick out from the relatively flat surface similar to we can observe from the real dissected case. Therefore, the height field will be inverted after projection to obtain a more representative visualization.

Finally, the volume data of the unfolded surface is obtained, and then surface rendering is used to visualize the resultant 3D model. Result and discussion of the unfolded surface will be presented in the next chapter.

CHAPTER

7

Results and Discussion

_____

In this section, the result of the unfolded colon surface will be discussed in detail. Since the CT dataset with positive diagnosis is not available, polyps are artificially added in the healthy colon in order to test the diagnostic ability of the unfolded view.

Four kinds of abnormalities are simulated here: sessile polyp, pedunculated polyp, mass and narrow segment (Fig. 7.1). The simulated sessile polyps are spherical. Some are sticking out from the inner surface of the colon, while others are partial submerged (Fig. 7.1(a)). Pedunculated polyps are attached to the surface through a stalk. As for mass, small carcinoma usually appear as a polypoid mass with a smooth outline, and a narrow segment is due to constriction or the thickening of colon wall. In this project, the first three types are generated artificially. One of the CT datasets has a narrow constriction due to suboptimal pre-scanning preparation and imaging process, we will use it as an example for the fourth type of abnormality.
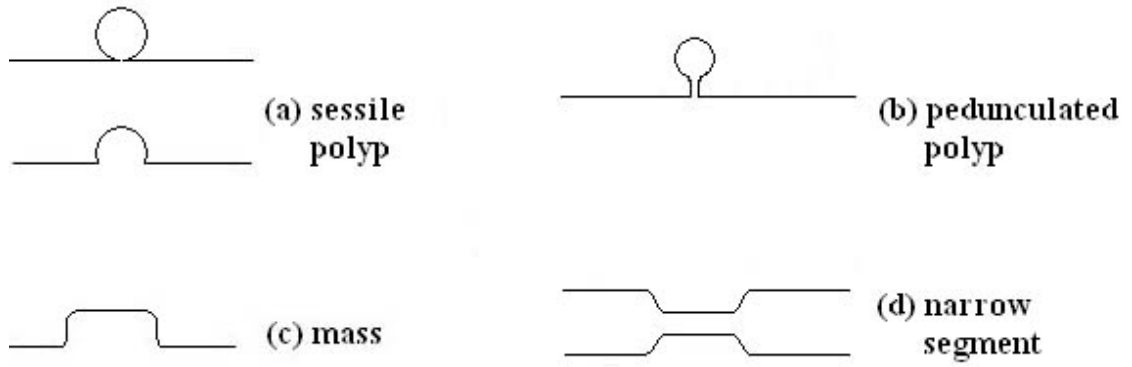
Figure 7.1 Four kinds of abnormalities inside the colon

As polyps smaller than 1cm have little probability to turn into cancer, most studies focus on detecting larger polyps. Polyps larger than 1cm are of clinical relevance. Therefore, the size of synthetic polyps is from about 1cm to 2cm in our experiments.

7.1 Experiment One

The colon dataset used here is the training dataset 1 (512x512x702) used in Chapter 4. The inter-pixel distance is 0.67mm x 0.67mm in the 2D slice, and the slice thickness is also resampled to be 0.67mm after segmentation. 10 artificial polyps which belong to the first three types are embedded in the segmented colon. Their types and sizes are described in Table 7.1. The medial axis and unfolded surface are obtained through the methods presented in the previous chapters.

The 3D view of the simulated polyps is provided in Fig. 7.2. As seen, some of the simulated polyps are close to the colon folds, and others are in the colon wall. For the two pedunculated polyps, one stalk (polyp P1) is short, while the other stalk (polyp P6) is longer.

Table 7.1 Descriptions of synthetic polyps

No.	Radius (mm)	Description
P1	5.9	Pedunculated polyp
P2	3.5	Sessile polyp
P3	6	Sessile polyp
P4	10 (height)	mass, height is 10mm, length is about 22mm
P5	7	Sessile polyp, two-third of a sphere
P6	6	Pedunculated polyp
P7	5	Sessile polyp
P8	8	Sessile polyp
P9	9	Sessile polyp, half-sphere
P10	10	Sessile polyp
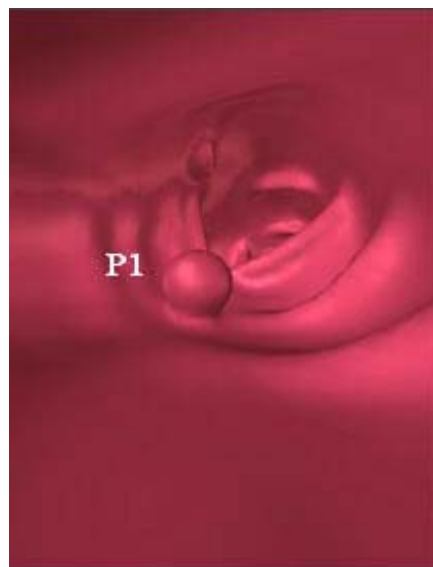
(a)   (b)
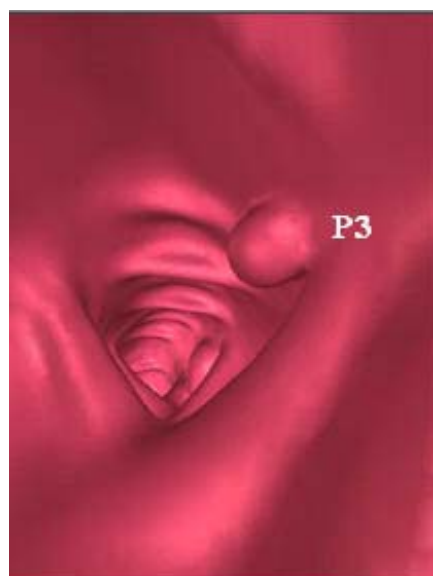
(c)

(d)
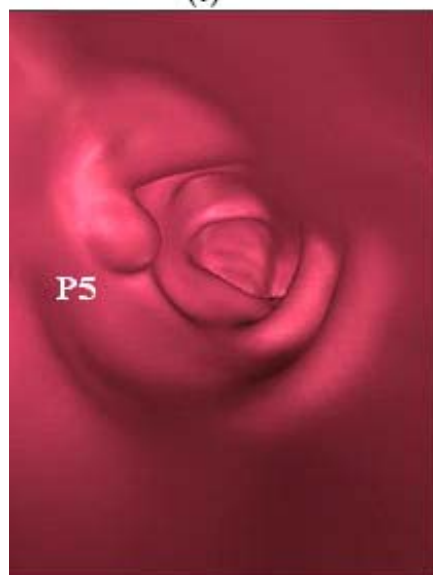
(e)
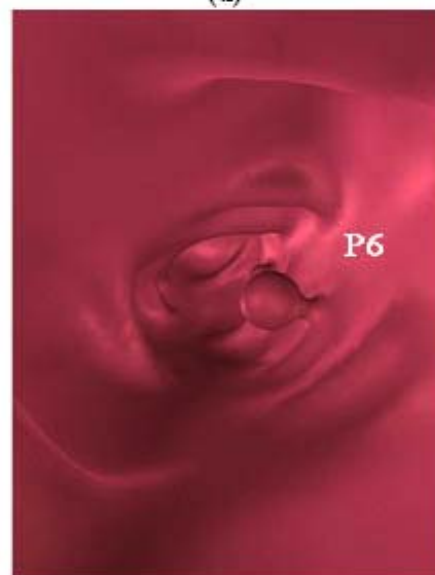
(f)

(g)

(h)
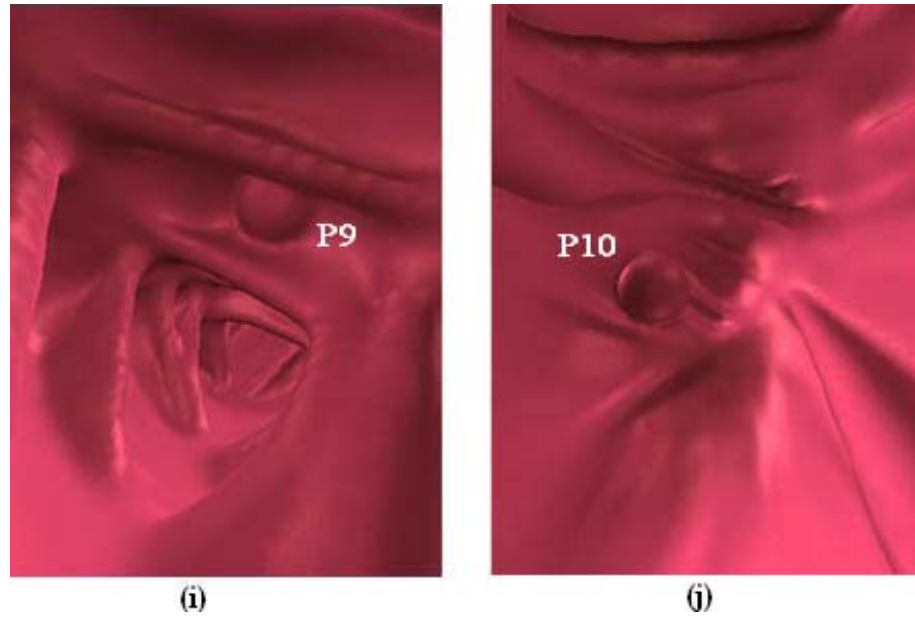
Figure 7.2 3D closed view of the 10 synthetic polyps

The unfolded surface is shown in Figs. 7.3, 7.4, 7.5, 7.6, 7.7 and 7.8. We explain in more detail two of the simulated polyps. For the mass P4, one end is connected with fold 1 and the other end is near to fold 2 as shown in Fig. 7.3(b). After unfolding, the mass is located between fold 1 and fold 2 with one end linked with fold 1, which can be obviously observed from Fig. 7.3(a).
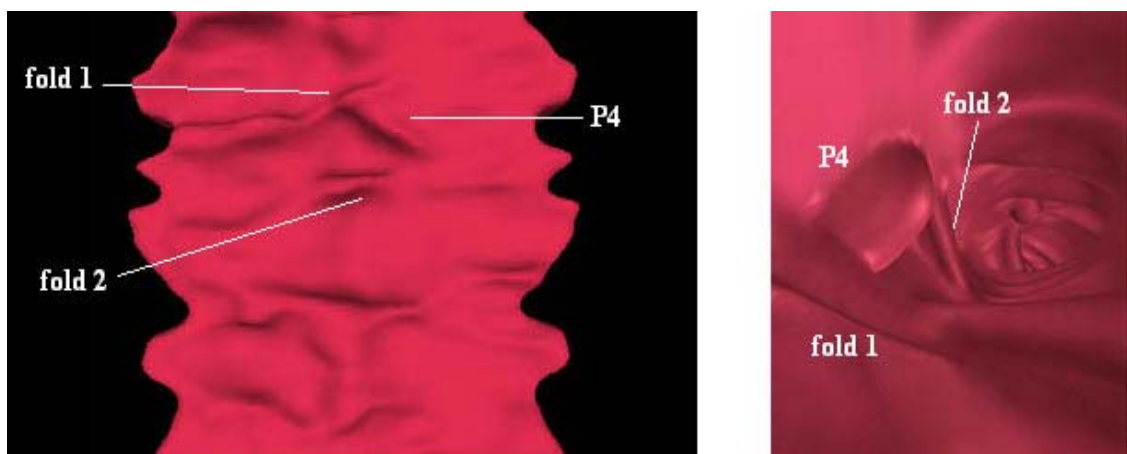
Figure 7.3 (a) Unfolded view of the mass P4, (b) 3D view of P4

The second example is the polyp P9. As illustrated in Fig. 7.4(b), the polyp is surrounded by several folds, among which fold 1 and fold 2 are the nearest. In the unfolded surface, fold 1 is above P9 and fold 2 is below P9, which are rightly unwrapped.
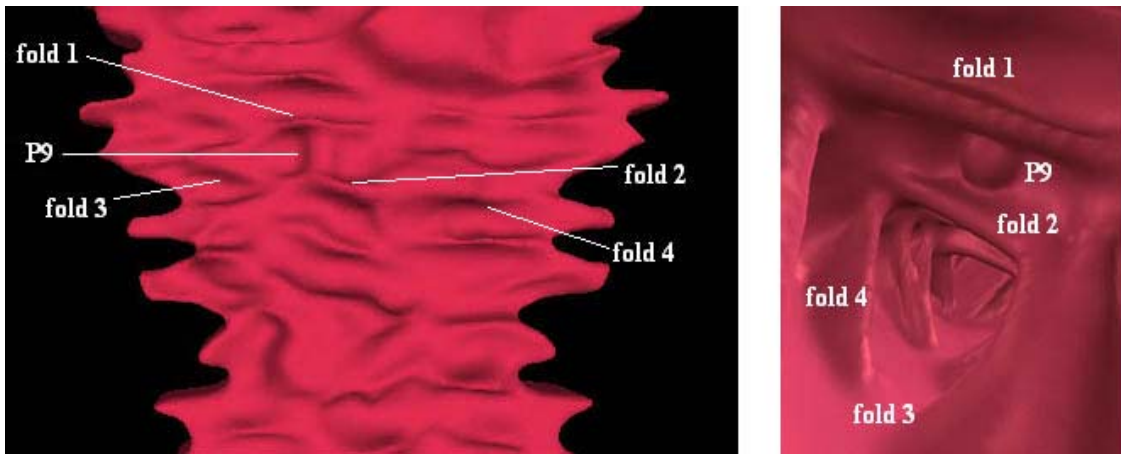
Fig 7.4 (a) Unfolded view of polyp P9, (b) 3D view of P9

The unfolded views of all the other polyps are presented below. Some polyps can be easily detected (Figure 7.5). Polyps P8 and P10 are big polyps with radius from 8mm to 10mm. As the biggest polyp, P10 can be easily found by virtual inspection. P8 hides behind a fold, which makes it less obvious compared to P10. Another aspect we can notice is that the surface around P10 is much wider than that around P8. That is because of the different radius of the colon at different location. As we have explained before, the diameter of the colon is the largest at the cecum end of the colon, and then decreases along the colon body (refer to Fig. 4.11). Here polyp P10 is located at the cecum, while the polyps P8 is located at the ascending colon next to the cecum. Therefore, the surface around P8 will be narrower than that around P10 after unfolding.
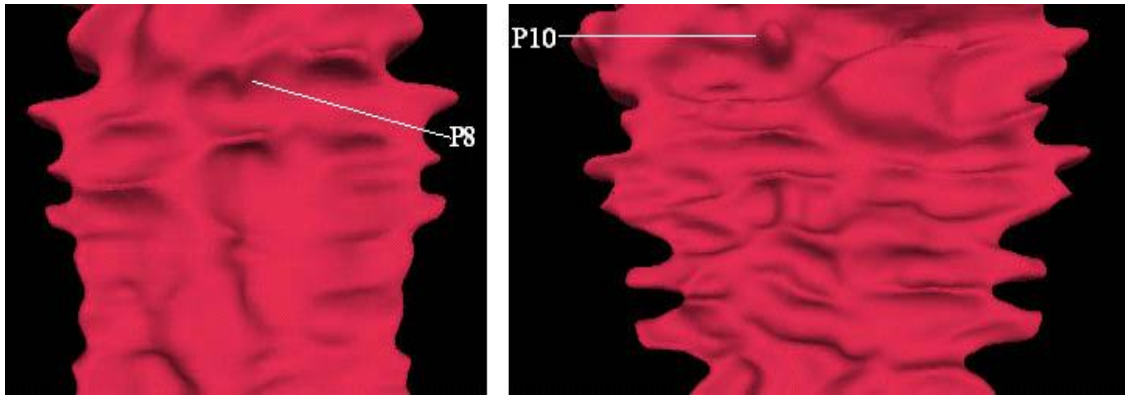
Figure 7.5 Unfolded view of P8 and P10

In Fig. 7.6, the polyp P1 and P3 are also detected with ease. Here P1 is a pedunculated polyp, but its stalk is too short to be sufficiently sampled by ray casting. Therefore, the shape of P1 is similar to that of sessile polyp, as is another stalked polyp P6 below. Polyp P2 is near to P1, and is almost unnoticeable. P2 is the smallest polyp ($r = 3.5$mm) among all the 10 synthetic polyps. By careful examination while rotating the surface for different view directions, a slight bulge can be found which will probably lead to the detection of P2. However, it is hard to differentiate it from surrounding structures under normal examination due to its small size.
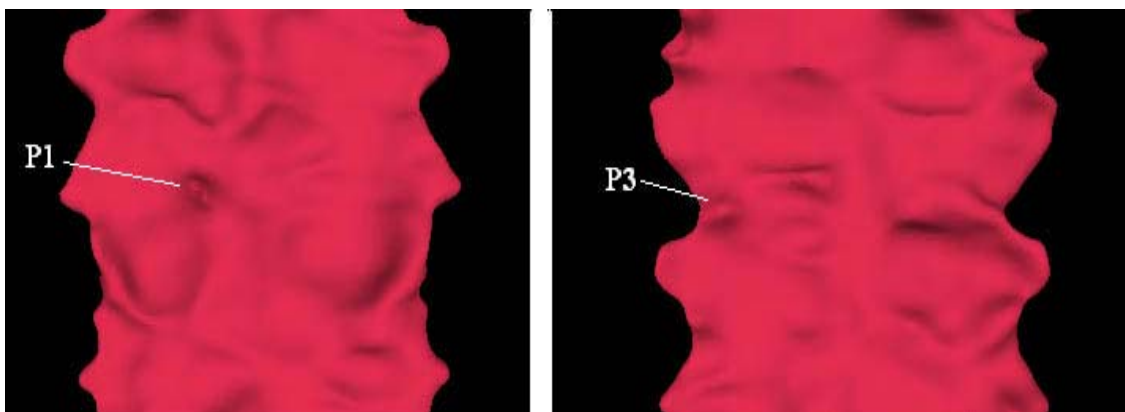
Figure 7.6 Unfolded view of P1 and P3

Polyp P5 and P6 can be inspected from Fig. 7.7(a). However, polyp P7 which is near P6 cannot be detected because it is located exactly at the edge of the surface. For this problem arising at the cutting edge of the 3D colon, an opposite view is generated to solve it as explained in section 6.4. For Fig. 7.7(a), the colon wall is unwrapped along a reference axis. If we set this reference axis to be the $0°$ position in the cross-sections, then the cutting edge should be around $180°$. Thus, another reference axis at $180°$ is applied for the surface unfolding. Then the cutting edge should be around $0°$. In this way, the surface around the cutting edge ($180°$) of the first case can be better visualized, as shown in Fig. 7.7(b). In this view, we manage to detect P7, although it is not as obvious as the other two due to its smaller size (r = 5mm).
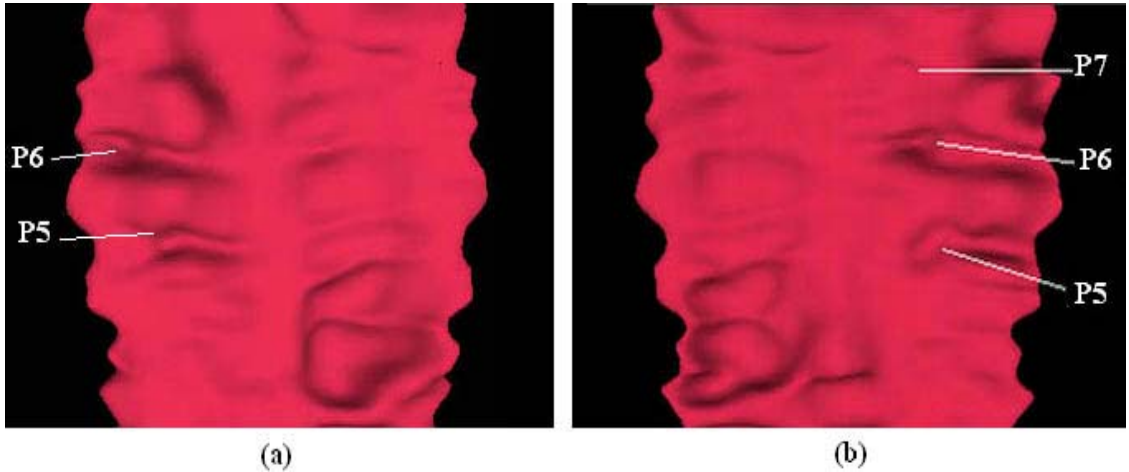
Figure 7.7 (a) Unfolded view of P5 and P6, (b) unfolded view of P5, P6 and P7 using the reference axis opposite to that of (a)

With the unfolded views in terms of two opposite reference axes, almost all the synthetic polyps can be visually detected except the smallest one P2 (r = 3.5mm). Sometimes the unwrapped surface needs to be rendered at a slightly different angle for a clearer view, e.g. the polyp will be higher than its neighboring area, which will be better observed in 3D environment provided by our system than the 2D image presented here. The entire colon wall is unfolded in Fig. 7.8, whose length is around 1.2 meter.

Figure 7.8 Unfolded view of the entire colon

7.2 Experiment Two

For this experiment, the dataset is the segmented dataset 2 (512x512x625) presented in section 4.4.2. The inter-pixel distance is 0.7mm x 0.7mm in 2D slice, and the slice thickness (1mm) is also resampled to be 0.7mm after segmentation. The medial axis and unfolded surface are obtained as presented in the previous chapters.

Here 5 lesions are simulated, including 2 sessile polyps, 2 pedunculated polyps and 1 mass. In addition, this dataset has a narrow segment probably caused by imperfect bowel preparation, which is treated as abnormal here. Thus, all of the four types of lesions mentioned before will be tested in this experiment. Their description is provided in Table 7.2.

Table 7.2 Descriptions of synthetic polyps

No.	Radius (mm)	Description
P1	8	sessile polyp
P2	5.1	sessile polyp
P3	6	pedunculated polyp
P4	5.5	pedunculated polyp
P5	10 (height)	mass, height is 10mm, length is 23mm
P6	N/A	narrow segment

The 3D endoluminal view of the above six lesions is shown in Fig. 7.9.
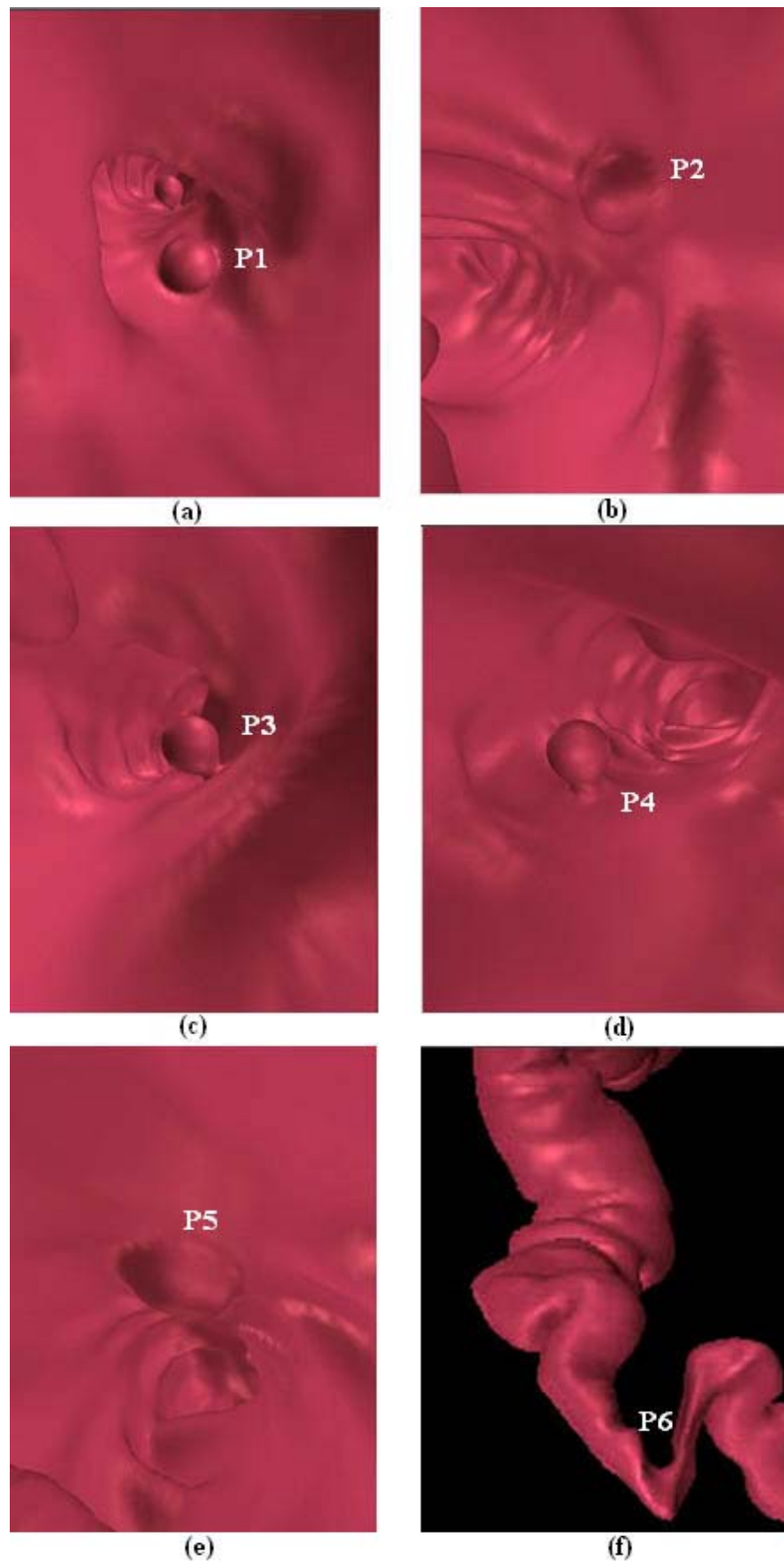
Figure 7.9 3D closed view of the 6 lesions

All the six lesions can be visually detected in this experiment. For example in Fig. 7.10, the polyp P2 and its surrounding folds are marked in both unfolded view and 3D endoluminal view.
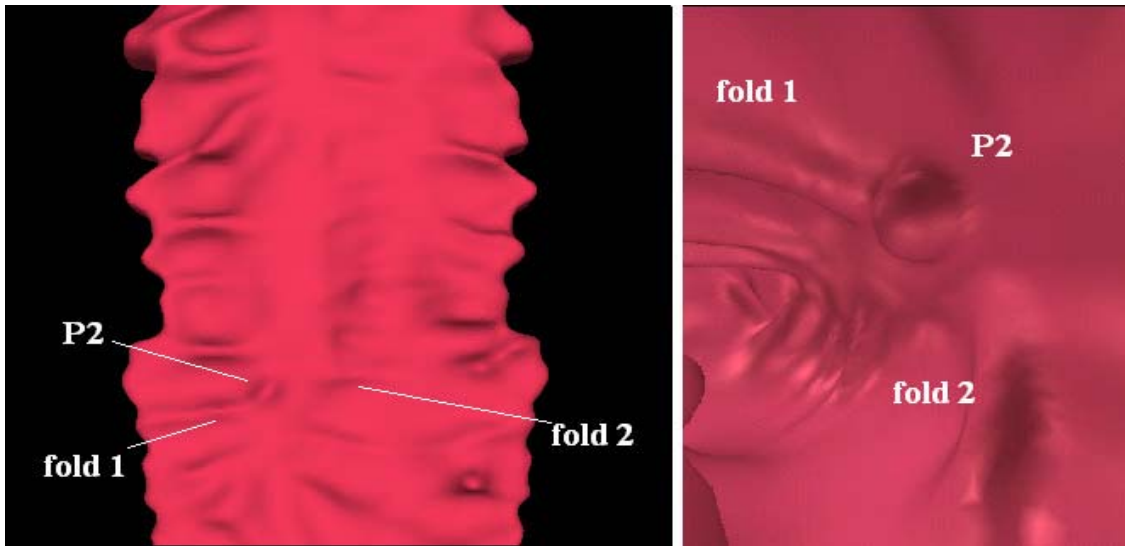
Figure 7.10 (a) Unfolded view of polyp P2, (b) 3D view of P2

The other polyps are all visualized and indicated in Fig. 7.11. As we can see, all the 5 embedded polyps can be successfully detected. The shape of pedunculated polyps is still similar to that of sessile polyps. The mass is obviously much bigger than the other polyps.
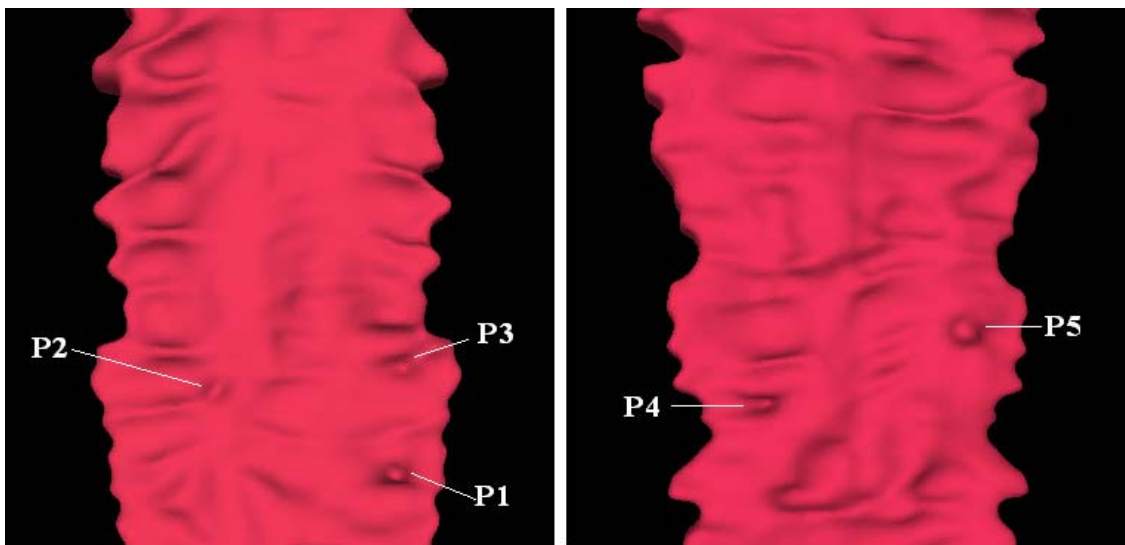
Figure 7.11 Unfolded view of polyps P1, P2, P3, P4 and P5

After unfolding, the narrow segment P6 appears to be a sudden slim surface as shown in Fig. 7.12. This kind of lesion is much easier to be detected compared with small polyps and mass.
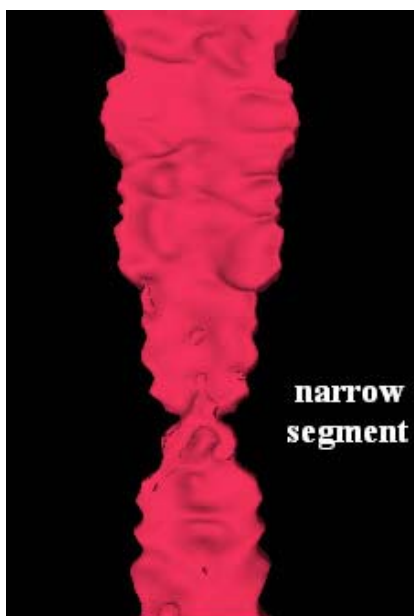
Figure 7.12 Unfolded view of the narrow segment P6

In this experiment, two unfolded views using two opposite reference axes for surface unfolding are combined to detect all the polyps. The unfolded surface of the entire colon is shown in Fig. 7.13. The total length is around 1.5 meter.
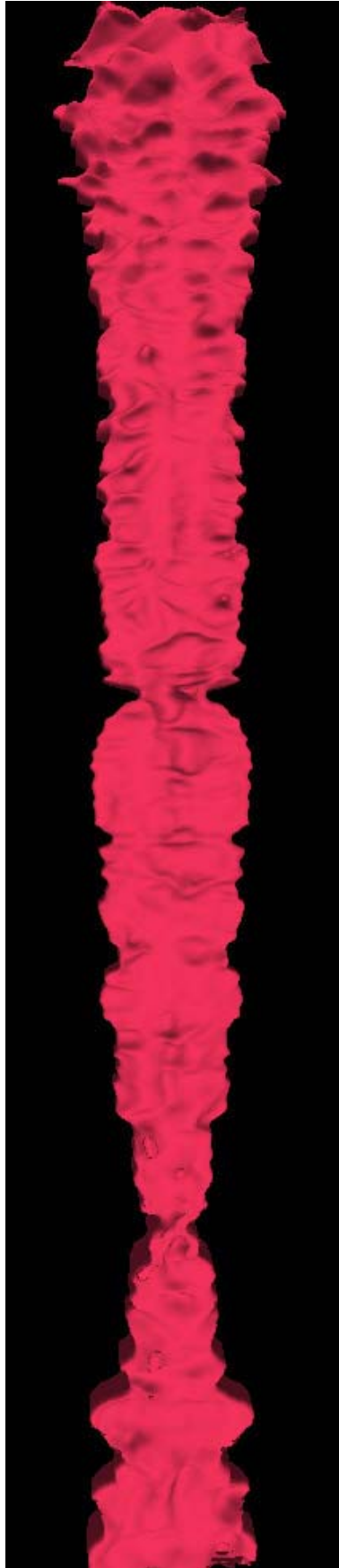
Figure 7.13 Unfolded view of the entire colon

From these two experiments, all the polyps larger than 1cm can be detected via visual inspection in the unfolded view. The small-sized polyp (such as P2 in the first experiment) is difficult to detect.

We note that the shape of the polyps in the unfolded view is somewhat different from their 3D views due to distortion caused in the unfolding process. The distortion is inevitable when an irregular 3D object is projected onto a 2D plane. However, the most important task is to detect abnormalities whereas the shape of the abnormalities is less important. Once abnormality is indicated real colonoscopy will be applied to remove it.

According to the current algorithms, the medial axis is desired to be the one that stays away from the surface as far as possible to ensure the centeredness of the virtual fly-through. This is to guarantee that the radiologist will not look outside or hit the inner surface when flying through the colon. For the unfolding case, the situation is slightly different. As a cross-section illustrated in Fig. 7.14(a), the distance from the center point is the same for every surface point ($r_0 = r_1 = ... = r_n$) if we suppose a simple case where the contour is a circle. When a polyp exists as in Fig. 7.14(d), the distance around the area of the polyp is obviously smaller (e.g. $r_0' < r_0$), while the normal area remains unchanged ($r_n' = r_n$) if the center point is the same as that in Fig. 7.14(a). To acquire a realistic surface, the height of unfolded surface in the middle column is inverted to produce the graph in the right column of Fig. 7.14. As a result, a flat surface with a bulge (Fig. 7.14(f)) will be obtained after unfolding this contour, which is the direct result that we are aiming for.
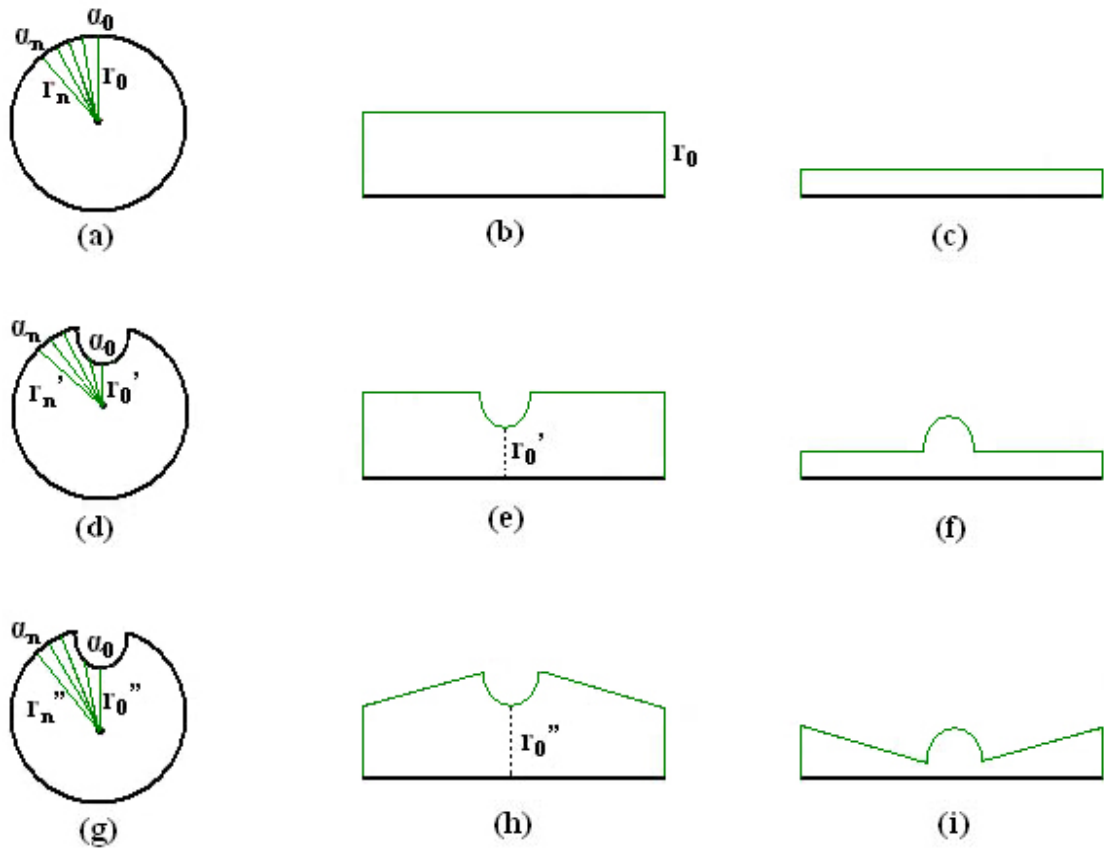
Fig 7.14 An example cross-section (a) without polyp, (d)with polyp but center not shifted, (g) with polyp but center shifted; (b)(e)(h) are corresponding unwrapped surface of (a)(d)(g); (c)(f)(i) are corresponding unwrapped surface after inverting surface height in (b)(e)(h).

However, since the medial axis is trying to stay in the center, the actual center point will shift away from the polyp as shown in Fig. 7.14(g). In this case, the relation of the distance value r between the points on the contour is changed totally as depicted in Fig. 7.14(h). After inverting the surface height, the resultant surface is far from what we desire. Although the bulge still exists, the portion of smooth surface will become uneven (Fig. 7.14(i)) especially when the real cross-section is not as smooth as this example. In addition, the bulge will be a little bit flattened as a result of decreased difference of height value between the polyp and its neighboring surface, which is caused by the shifting of the center. Therefore, this surface is not ideal. Future research will be needed for the development of new algorithms to acquire a global centerline

not influenced by local surface features.

Table 7.3 shows the calculation time of the surface unfolding for the two experiments. The program is executed using a Pentium Ⅳ 2.4GHz machine. To improve the computational efficiency, the datasets are reduced to be a volume that is just sufficient to cover the colon. Distance transform timing includes computation of two distance maps: one is the distance map from the medial axis, and the other is the distance map from the colon surface. The rest presents the timing for the three main procedures in the unfolding process: ray casting, snakes and projection onto 2D grids.

Table 7.3 Computation time for the surface unfolding

Dataset	Dataset after compression	Distance Transform (min)	Ray Casting (min)	Snakes (min)	Projection (min)	Total (min)
Colon data 1 (512x512x702)	392x234x505	8.70	2.02	0.28	0.02	**11.02**
Colon data 2 (512x512x625)	398x232x578	8.15	2.08	0.22	0.03	**10.48**

Computation time depends on the resolution of the dataset and the size of the object. As we can see from Table 7.3, the three phases of unfolding are very fast. While most time is spent in distance map calculation, because it is an iterative procedure and requires huge computer memory. In addition, the distance transform here adopt a Euclidean metric which highly increases the computational time. In total, the time of the whole process is around 10 minutes, which is fairly acceptable for clinical use.

<div align="right">

CHAPTER
8

</div>

Conclusion and Future Work

_____

8.1 Conclusion

In this project we have developed a virtual colonoscopy system which can be used to facilitate clinical diagnosis for colorectal abnormalities in the near future. This system includes several phases for offline processing: near-automatic segmentation, automatic medial axis extraction and automatic surface unfolding. The online visualization is able to provide two diagnostic approaches: fly-through navigation and virtual dissection, with the latter being the focus of this project.

In the segmentation stage of this system, simply thresholding or region growing cannot extract the colon body. There are three main reasons: existence of fluid residues inside the colon, the partial volume effect between colon air and fluid residues, and the overlap of the intensity value between colon and some other organs. Therefore, we combine thresholding and 3D region growing to solve the above problem. The results

are good.

For the medial axis extraction, good centeredness and connectivity are required to ensure that the user will not hit the surface in the fly-through navigation, and to ensure that the colon wall is well unfolded. The method we used is based on distance transform. Two distance transforms are used. One is the distance transform from a single point which allows the extraction of the shortest path inside the colon, while the other is the distance transform from the colon surface which improves the centeredness of the axis. The excellent results from the three training datasets affirmed the performance of this algorithm.

The focus of this project, the surface unfolding, aims to enable the physician to quickly inspect the whole inner surface of the colon in one view. The method is to first sample the colon surface in the form of a series of cross-sections, and then to unfold them onto a plane. To avoid intersections of adjacent cross-sections at high curvature areas, ray casting is applied to obtain curved cross-sections based on the distance map from the colon surface. A two-time snake algorithm is then proposed to refine the cross-sections using two energy functions. Finally the cross-sections are projected onto the plane to get the unfolded surface. The algorithm has been tested with two colon datasets. To examine the ability of detecting abnormal structures, several synthetic polyps are inserted into the healthy colon data. Results show that polyps larger than 1cm can be successfully detected through visual inspection. The system is shown to be promising.

8.2 Future Work

As we discussed in the previous chapter, the problem of the medial axis remains to be solved. The current algorithms proposed to extract the medial axis with high centeredness, which is necessary for fly-through navigation. However, we hope that the medial axis is not affected by local curvature in order to acquire an ideal surface with obvious local structure in the surface unfolding process. Therefore, new studies need to be initiated on this aspect.

Improvement of the unfolding algorithm to minimize the geometric distortion is another subject of future work. In addition, future studies may also be needed to improve the ability to detect small-sized polyps. Automatic polyp detection is also under research, which could greatly accelerate and improve the diagnosis.

Most of the studies are on CT colon images. MR colonography is not widely accepted due to its low resolution and high cost. However, it is radiation-free. Another advantage of MRI is its capability to visualize different contrast in soft tissue, which is an important aspect for inspecting and confirming colorectal abnormalities. Therefore, future efforts should be made to extend the developed colonoscopy system to MR colonoscopy.

The datasets used in this project are CT images of healthy colon. In order to be deployed in clinical diagnosis, the developed system should be tested with more datasets of real pathology in the future.

References

[1] Jemal A., Murray T., Samuels A., Ghafoor A., Ward E. and Thun M.J. Cancer statistics 2003. *CA: A Cancer Journal for Clinicians*, vol. 53, pp. 5-26, 2003.

[2] Muto T., Bussey H.J., and Morson B.C. The evolution of cancer of the colon and rectum. *Cancer*, vol. 36, pp.2251-2270, 1975

[3] Kosary C.L. and others (eds). SEER Cancer Statistics Review, 1973-1992. Bethesda, Md.: National Cancer Institute, 1995, NIH Pub. No. 94-2789.

[4] Source: Digestive disease library – colon and rectum, Gastroenterology & Hepatology Resource Center, The Johns Hopkins Medical Institutions. http://hopkins-gi.nts.jhu.edu/pages/latin/templates/index.cfm?pg=disease1&organ=6&disease=36&lang_id=1

[5] Gibbons L., Waters C., Mao Y. et al. Trends in colorectal cancer incidence and mortality. *Health Reports*, vol. 12, No. 2, pp. 41-55, 2001.

[6] http://www.surgicom.co.za/colonoscopy.htm

[7] Sorantin E., et al. Virtual dissection of the colon. In *3D Image Processing – Techniques and Clinical Applications*, ed by D.Caramella and C.Bartolozzi, Springer, pp.197-209, 2002.

[8] Source: Virtual colonoscopy, Department of Radiology, NYU School of medicine. http://virtualcolonoscopy.med.nyu.edu/image/image1.html

[9] Mendelson R.M., Foster N.M., Edwards J.T. et al. Virtual colonoscopy compared with conventional colonoscopy; a developing technology. *The Medical Journal of Australia*, vol. 173, pp. 472-475, 2000.

[10] Fletcher J.G., Johnson C.D., Welch T.J. et al. Optimization of CT colonography technique: prospective trial in 180 patients. *Radiology*, vol. 216, pp. 704-711, 2000.

[11] Fenlon H.M., Nunes D.P., Schroy P.C. et al. A comparison of virtual and conventional colonoscopy for the detection of colorectal polyps. *The New England Journal of Medicine*, vol. 341, pp. 1496-1503, 1999.

[12] Yee J., Akerkar G.A., Hung R.K. et al. Colorectal neoplasia: performance characteristics of CT colonography for detection in 300 patients. *Radiology*, vol. 219, pp. 685-692, 2001.

[13] Hopper K.D., Khandelwal M., Thompson C. CT colonoscopy: experience of 100 cases using volumetric rendering. In *Proceedings SPIE*, vol. 4321, pp. 489-494, 2001.

[14] Yee J, Hung R.K., Steinauer-Gebauer A.M. Prospective comparison of CT colonography and conventional colonoscopy for colorectal polyp detection. *Radiology (suppl.)*, 213:340, 1999.

[15] Vining D. and Gelfand D. Noninvasive colonoscopy using helical CT scanning, 3D reconstruction, and virtual reality. *Proceedings of 23rd Annual Meeting of the Society of Gastrointestinal Radiologists*, Maui, Hawaii, pp.70, 1994.

[16] Johnson C.D., Hara A.K. and Reed J.E. Virtual endoscopy: what's in a name? *American Journal of Roentgenology*, vol. 171, pp.1201-1202, 1998.

[17] Luboldt W., Bauerfeind P., Wildermuth S., et al. Colonic masses: detection with MR colonography. *Radiology*, vol. 216, pp. 383-388, 2000.

[18] Pappalardo G., Polettini E., Frattaroli F.M., et al. Magnetic resonance colonography versus conventional colonoscopy for the detection of colonic

endoluminal lesions. *Gastroenterology*, vol. 119, pp. 300-304, 2000.

[19] Yee J, et al. Comparison of supine and prone scanning separately and in combination at CT colonography. *Radiology*, vol. 226, pp. 653-661, 2003.

[20] Laghi A., Pavone P., Panebianco V., Catalano C., Baeli I. and Passariello R. Spiral CT colography and volume-rendered virtual colonoscopy: an initial prospective study. *European Radiology*, 9: 816, 1999.

[21] Vining D. Optimizing bowel preparation. *First International Symposium on Virtual Colonoscopy*, Boston, Mass., Boston University Press, pp. 79-80, 1998.

[22] Morrin M.M. and LaMont J.T. Screening virtual colonoscopy – ready for prime time? *The New England Journal of Medicine,* vol. 349, pp. 2261-2264, 2003.

[23] Winawer S.J., Fletcher R.H., Miller L. et al. Colorectal cancer screening: clinical guidelines and rationale. *Gastroenterology*, vol. 112, pp. 594-642, 1997.

[24] Vos F., Serlie I., Gelder R.V, Stoker J., Vrooman H. and Post F. A review of technical advances in virtual colonoscopy. *Proceedings of the 10th World Congress on Medical Informatics – MedInfo 2001,* ed by Patel VL, Rogers R and Haux R. IOS Press, Amsterdam, pp. 938-942, 2001.

[25] Mendelson R.M. and Forbes G.M. Computed tomography colonography (Virtual Colonoscopy): Review. Australasian Radiology, vol. 46, pp. 1-12, 2002.

[26] Serlie I., Vos F., et al. Improved visualization in virtual colonoscopy using image-based rendering. *IEEE TCVG Symposium on Visualization, Conference Proceddings,* pp. 137-146, 2001.

[27] Vos F, Gelder R.V., Serlie I, et al. Three-dimensional display modes for CT colonography: conventional 3D virtual colonoscopy versus unfolded cube

projection. *Radiology*, vol. 228, pp. 878-885, 2003.

[28] Lakare S, Chen D, Li L, et al. Electronic colon cleansing using segmentation rays for virtual colonoscopy. *SPIE Medical Imaging, Physiology and Function from Multidimensional Images*, vol. 4683, pp. 412-418, San Diego, CA, USA, 2002.

[29] Hohne K.H. and Hanson W.A. Interactive 3D segmentation of MRI and CT volumes using morphological operations. *Journal of Computer Assisted Tomography*, vol. 16, pp. 285-294, 1992.

[30] Vilanova A., König A., and Gröller E. VirEn: A virtual endoscopy system. *Machine Graphic & Vision*, vol. 8, pp. 469-487, 1999.

[31] Wyatt C.L., Ge Y., Vining D.J.. Automatic segmentation of the colon for virtual colonoscopy. *Computerized Medical Imaging and Graphics*, vol. 24, pp. 1-9, 2000.

[32] Chen D., Liang Z., Wax M.R., Li L., Li B. and Kaufman A. A novel approach to extract colon lumen from CT image for virtual colonoscopy. *IEEE Trans. on Medical Imaging*, vol. 19, pp. 1220-1226, 2000.

[33] Lakare S., Wan M., Sato M. and Kaufman A. 3D digital cleansing using segmentation rays. *IEEE Visualization 2000 Proceedings*, pp. 37-44, Salt Lake City, Utah, USA.

[34] Sato M., Lakare S., Wan M., et al. An automatic colon segmentation for 3D virtual colonoscopy. *IEICE Trans. Information and Systems*, vol. E84-D, pp. 201-208, 2001.

[35] Ge Y., Stelts D. and Vining D. 3D skeleton for virtual colonoscopy. In *Proceedings of the 4th International Conference on Visualization in Biomedical Computing*, pp. 449-454, 1996.

[36] McFarland E.G., Wang G.., Brink J.A., Balfe D.M., Heiken J.P. and Vannier M.W. Spiral computer tomographic colonography: determination of the central axis and digital unraveling of the colon. *Academy of Radiology*, vol. 4, pp. 367-373, 1997.

[37] Ge Y., Stelts D., Wang J. and Vining D. Computing the centerline of a colon: a robust and efficient method based on 3-D skeleton. *Journal of Computer Assisted Tomograhpy*, vol. 23, no. 5, pp. 786-794, 1999.

[38] Paik D., Beaulieu C., Jeffery R., Rubin G. and Napel S. Automatic flight path planning for virtual endoscopy. *Medical Physics*, vol. 25, no. 5, pp. 629-637, 1998.

[39] Bouix S., Siddiqi K., Tannenbaum A. Flux driven automatic centerline extraction. *Medical Image Analysis*, 2004, in press.

[40] Samara Y., Fiebich M., Dachman A.H., Kuniyoshi J.K., Doi K. and Hoffmann K.R. Automated calculation of the centerline of the human colon on CT images. *Academic Radiology*, vol. 6, pp. 352-359, 1999.

[41] Zhou Y. and Toga A.W. Efficient skeletonization of volumetric objects. *IEEE Trans. Visualization and Computer Graphics*, vol. 5, no. 3, pp. 196-209, 1999.

[42] Chen D., Li B., Liang Z., Wan M., Kaufman A. and Wax M. A tree-branch searching multiresolution approach to skeletonization for virtual endoscopy. *Proc. SPIE Medical Imaging*, vol. 3979, pp. 726-734, 2000.

[43] Bitter I., Kaufman A. and Sato M. Penalized-distance volumetric skeleton algorithm. *IEEE Transactions on Visualization and Computer Graphics*, vol. 3, pp. 195-206, 2001.

[44] Wan M., Liang Z., Ke Q., Hong L., Bitter I. and Kaufman A. Automatic centerline extraction for virtual colonoscopy. *IEEE Transactions on Medical Imaging*, vol. 21, no. 12, 2002.

[45] Wang G. and Vannier M.W. GI tract unraveling by spiral CT. In *Proceedings SPIE.*, vol. 2434, pp. 307-315, 1995.

[46] Wang G., McFarland E.G, Brown B., Vannier M.W. GI tract unraveling with curved cross sections. *IEEE Transaction on Medical Imaging*, vol. 17, pp. 318-322, 1998.

[47] Wang G., Dave S.B, Brown B.P, Zhang Z., McFarland E.G, Haller J.W and Vannier M.W. Colon unraveling based on electrical field: recent progress and further work. In *Proceedings SPIE*, vol. 3660, pp. 125-132, 1999.

[48] Haker S., Angenent S., Tannenbaum A. and Kikinis R. Nondistorting flattening maps and the 3D visualization of colon CT images. *IEEE Transactions on Biomedical Engineering*, vol. 19, pp. 665-671, 2000.

[49] Bartroli A.V., Wegenkittl R., König A., Gröller E. and Sorantin E. Virtual colon flattening. In *VisSym'01 Joint Eurographic – IEEE TCVG Symposium on Visualization*, *Conference Proceedings*, pp. 127-136, 2001.

[50] Bartroli A.V, Wegenkittl R., König A. and Gröller E. Nonlinear virtual colon unfolding. In *IEEE Visualization 2001, Conference Proceedings*, pp. 411-418, 2001.

[51] Yeo E.T. *Virtual Colonoscopy Software*. B.Eng Thesis, National University of Singapore, 2004.

[52] Gonzalez R.C. and Woods R.E. *Digital Image Processing*. pp. 604, Prentice Hall, 2002.

[53] Poston T., Wong T., Heng P. Multiresolution isosurface extraction with adaptive skeleton climbing. *Eurographics '98*, vol. 17, issue 3, 1998.